Theoretical and Applied Fracture Mechanics 147 (2026) 105820

Contents lists available at ScienceDirect

Theoretical and Applied Fracture Mechanics

journal homepage: www.elsevier.com/locate/tafmec

A probabilistic fatigue life model for the evaluation of casting defects in a nickel-based superalloy under high temperature LCF-loading

Jan Radners [a,*], Christoph Schweizer [a], Stefan Eckmann [a], Britta Bilger [a], Michael Schlesinger [a], Christian Amann [b], Peter Gumbsch [a,c], Kai Kadau [d]

[a] *Fraunhofer Institute for Mechanics of Materials IWM, Freiburg, Germany*
[b] *Siemens Energy Global GmbH & Co. KG, Mülheim a. d. R., Germany*
[c] *Karlsruhe Institute of Technology (KIT), Institute for Applied Materials, Karlsruhe, Germany*
[d] *Siemens Energy Inc., Charlotte, NC, United States*

ARTICLE INFO

Keywords:
Low cycle fatigue
Lifetime prediction
Probabilistic modeling
Material defects
High temperatures
Nickel-based superalloy
Turbine blade

ABSTRACT

This work presents a physically based probabilistic model for LCF life of the conventional cast (CC) nickel-based superalloy MAR-M247. The model explicitly accounts for the effects of casting defects. Over 100 LCF tests were conducted at 850 °C and 950 °C on specimens with and without defects. Specimens were extracted from turbine blades that had manufacturing-related casting defects. Additionally, artificial defects were introduced into initially defect-free specimens. A multi-stage CT- and μCT-based specimen extraction strategy was developed to precisely position casting defects within specimens. Defects were parameterized orthogonally to the loading direction based on their size, shape and orientation using SEM fractography. For all tested strain ranges, a dominant influence of defect size on fatigue life was found. The effects of defect shape and orientation were small in comparison. Significant scatter of material parameters was observed experimentally. Electron backscatter diffraction (EBSD) revealed significant variations in grain size and orientation depending on the specimen extraction position. The model accounts for this by using individual values for stress ratio R_σ and Young's modulus E. LCF fatigue life was modeled using an approach based on the cyclic crack tip opening displacement $\Delta CTOD$. Defect size was accounted for as an initial crack length based on the Feret diameter d_{Feret} of each defect. Additionally, an El Haddad-type threshold term was used to account for defect size dependence in the high-cycle regime. Validation against experimental data showed robust prediction accuracy across all defect types, defect sizes, specimen geometries, temperatures, and strain ranges. Model inaccuracies arising from the fracture mechanics based approximation solution were estimated analytically. For defects large compared to the specimen geometry, a tendency towards more conservative fatigue life assessment was shown. A probabilistic framework was established using Monte Carlo simulations. Material scatter was modeled using experimentally derived distributions for E and R_σ. Fatigue life distributions were quantified under realistic operating temperatures and loads. The results support risk-based maintenance and optimized gas turbine operation in modern decarbonized energy systems.

1. Introduction

Addressing anthropogenic climate change is a great challenge that requires the integration of renewable energy resources into the grid [1]. The fluctuating availability of these renewable energies, however, makes the addition of highly flexible power generation systems necessary. Gas turbines, as depicted in Fig. 1(a), are particularly well-suited for providing large amounts of energy on short notice due to their flexible operation capabilities [2]. They can contribute to bridging supply gaps from renewables, support peak load management, and help maintain grid stability. Gas turbines exhibit high efficiencies in combined cycles and are capable of sustainably providing energy using alternative fuels (e.g., hydrogen-rich fuels or biofuels) [3,4]. However, an increasingly flexible use of gas turbines results in a significant increase in the number and speed of transient load cycles e.g., start-stop-cycles. This considerably increases the low-cycle fatigue (LCF) loading of critical rotating gas turbine components, such as turbine blades as depicted in Fig. 1(b). For such components, a robust evaluation of the fatigue lifetime is required to ensure reliable and safe gas turbine operations. Highly efficient turbine blades are typically produced by casting. This process can introduce imperfections like

* Corresponding author.
E-mail address: jan.radners@iwm.fraunhofer.de (J. Radners).

https://doi.org/10.1016/j.tafmec.2026.105820
Received 8 May 2026; Received in revised form 18 June 2026; Accepted 12 July 2026
Available online 20 July 2026

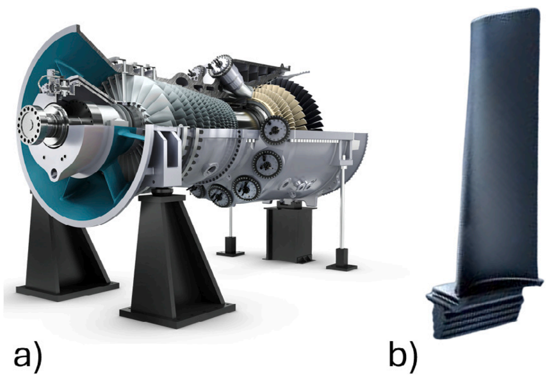

Fig. 1. (a) Siemens Energy SGT-9000HL GT, (b) Turbine blade. © 2023 Siemens Energy.

unfavorable grain sizes or casting pores [5]. These defects can reduce the life of the components. In particular, shrinkage pores can lead to nucleation of fatigue cracks [6]. Although counter measures such as hot isostatic pressing (HIP) can improve fatigue performance [7] and significantly reduce defects in size [8], defects are often not entirely removable [9,10] and the process is ineffective for defects that have a connection to the surface of the part. Furthermore, non-destructive testing cannot quantify the exact defect sizes and shapes, nor can it guarantee that no defects are present. Previous work [11] reported a series of low-cycle fatigue tests, primarily on defect-free specimens, with additional tests on specimens containing artificial defects, and proposed an initial deterministic model. Building on this, subsequent work [12] provided first insights into the influence of defect size and morphology on LCF performance at high temperatures. Completing this series of studies, the present work introduces extensive additional experimental data, detailed analyses, and a physics-based probabilistic model capable of predicting the LCF life of MAR-M247 at high temperatures while accounting for casting defects.

2. Theoretical background

2.1. Deterministic fatigue life modeling

In the literature, numerous phenomenological approaches exist for describing the fatigue life under cyclic loading. Well known approaches for example are the ones by Smith, Watson and Topper [13] or Coffin [14] and Manson [15]. Additionally, a large variety of mechanism-based approaches exist [16] that are based on the fact that fatigue life of a cyclically loaded specimen is determined by the formation and growth of small cracks. In the LCF regime (i.e., for high load amplitudes) fatigue cracks usually initiate early and short crack growth dominates the fatigue life [17–19]. Based on a variety of experimental studies (e.g., Neumann [20]), physical fracture mechanics based fatigue crack growth models were suggested that describe the crack growth increment per cycle $\mathrm{d}a/\mathrm{d}N$ for cracks under mode I loading using the cyclic crack tip opening displacement $\Delta CTOD$:

$$\frac{\mathrm{d}a}{\mathrm{d}N} = \beta \Delta CTOD^{B}, \tag{1}$$

where the factor β can be considered a material constant for polycrystalline materials and B is an additional material dependent exponent, following Schweizer [21] and Serrano et al. [22]. For a short semicircular surface crack with the depth a, $\Delta CTOD$ can be estimated as in [23]:

$$\Delta CTOD = d_{\mathrm{n}'} \frac{Z_{\mathrm{D}}}{\sigma_{\mathrm{cy}}} a. \tag{2}$$

Here, σ_{cy} denotes the cyclic yield stress. Eq. (2) is based on a relation between the J-integral and the crack tip opening displacement $CTOD$ formulated by Shih [24] and its adaptation to cyclic parameters [25]. Details on its derivation can be found in [21,26]. The parameter $d_{\mathrm{n}'}$ originates from the Hutchinson-Rice-Rosengren crack tip fields (introduced by Hutchinson [27], Rice and Rosengren [28]) and was tabulated by Shih [24] as a function of the hardening exponent n' for a power-law hardening material (e.g., Ramberg–Osgood [29]). For $d_{\mathrm{n}'}$ the following fit by Schweizer [21] is available:

$$d_{\mathrm{n}'} = 0.78627 - 3.41692n' + 6.11945n'^{2} - 4.2227n'^{3}. \tag{3}$$

According to Kumar et al. [30], the cyclic J-integral ΔJ can be approximated by the sum of an elastic and plastic contribution:

$$\Delta J = \Delta J_{\mathrm{el}} + \Delta J_{\mathrm{pl}}. \tag{4}$$

The damage parameter Z_{D} by Heitmann [31] can be understood as the normalized cyclic J-integral $\Delta J_{\mathrm{eff}}/a$, which additionally accounts for crack closure effects, as described by Elber [32]. Following Riedel [33], based on Eq. (4), Z_{D} can be written as:

$$Z_{\mathrm{D}} = Z_{\mathrm{D,el}} + Z_{\mathrm{D,pl}} = 1.45 \frac{\left(\Delta\sigma_{\mathrm{eff}}\right)^{2}}{E} + 2.4 \frac{\Delta\sigma \Delta\varepsilon_{\mathrm{pl}}}{\sqrt{1 + 3n'}}, \tag{5}$$

where E is Young's Modulus and $\Delta\sigma$ and $\Delta\varepsilon_{\mathrm{pl}}$ are the stress range and plastic strain range, respectively. Both can be evaluated from a hysteresis loop. $\Delta\sigma_{\mathrm{eff}}$ is the effective stress range and accounts for crack closure effects. Newman [34] suggested the following relation for $\Delta\sigma_{\mathrm{eff}}$:

$$\Delta\sigma_{\mathrm{eff}} = \sigma_{\max} - \sigma_{\mathrm{op}}, \tag{6}$$

where the crack opening stress σ_{op} is calculated according to Eq. (7) and $\sigma_{\max}$ is the maximum stress occurring in a loading cycle.

$$\frac{\sigma_{\mathrm{op}}}{\sigma_{\max}} = \begin{cases} A_0 + A_1 R_\sigma + A_2 R_\sigma^2 + A_3 R_\sigma^3 & \text{for } R_\sigma \geq 0, \\ A_0 + A_1 R_\sigma & \text{for } -1 \leq R_\sigma < 0. \end{cases} \tag{7}$$

R_σ denotes the cyclic stress-ratio and is defined by the minimum stress $\sigma_{\min}$ and the maximum stress $\sigma_{\max}$ in a load cycle:

$$R_\sigma = \frac{\sigma_{\min}}{\sigma_{\max}}. \tag{8}$$

In Eq. (7) the A_i with $i = 0, 1, 2, 3$ are calculated with:

$$A_0 = \left(0.825 - 0.34\alpha + 0.05\alpha^2\right) \left[\cos\left(\frac{\pi\sigma_{\max}}{2\sigma_{\mathrm{y}}}\right)\right]^{\frac{1}{\alpha}}, \tag{9}$$

$$A_1 = \frac{(0.415 - 0.071\alpha)\,\sigma_{\max}}{\sigma_{\mathrm{y}}}, \tag{10}$$

$$A_2 = 1 - A_0 - A_1 - A_3, \tag{11}$$

$$A_3 = 2A_0 + A_1 - 1. \tag{12}$$

Here, σ_{y} is the yield stress and α is a constraint factor with $\alpha = 1$ for a plane stress state and $\alpha = 3$ for a plane strain state.

To assess the fatigue life of a component in the presence of a defect or crack (cyclic damage tolerance), models usually assume an initial flaw at a critical location. Fatigue life is then calculated based on long crack growth [35]. Engineering fracture mechanics, such as linear elastic fracture mechanics (LEFM), are widely used for this purpose. An assessment of whether the component will fail or not during its lifetime, can be made by comparing the minimum computed life with the design target life. To account for uncertainties in the computed fatigue crack growth life, safety factors are often applied [35]. Several authors [36–40] used elastic–plastic fracture mechanics based on the effective cyclic J-integral ΔJ_{eff} in a comparable form to Eq. (5), to assess the LCF lifetime of additively manufactured materials by converting the size of preexisting defects into an initial crack size using Murakami's [41] $\sqrt{\text{area}}$-parameter.

2.2. Microstructural influence on fatigue

The grain structure, including grain size and orientation, significantly affects fatigue crack initiation and growth [42–46]. In single crystals, the LCF life strongly depends on the crystal orientation, resulting in differences in the fatigue life of more than an order of magnitude [47]. The deformation behavior of nickel-based superalloys also strongly depends on the manufacturing process and the resulting microstructure [19]. Depending on the grain orientation, nickel-based superalloys exhibit tension-compression asymmetries [48], for example due to an orientation dependence of the tensile and compressive yield stresses [49]. When the grain size is comparable to typical defect sizes, crack initiation may not be solely determined by the properties of the defects and the location of crack initiation may only partially align with regions of maximum mechanical load derived from a structural-mechanical evaluation [22]. This phenomenon is often observed in fracture mechanics specimens made from coarse-grained nickel alloys. When subjected to cyclic loading in laboratory settings, these specimens sometimes fail outside the previously introduced geometric notches [22]. This occurs because individual grain orientations can lead to stress concentrations that are equivalent to or even exceed those in the introduced notches. For notched specimens made from René 80, Engel et al. [50] found that a crystallographic texture which is beneficial for smooth specimens can lose its advantage, because the resulting stiffness distribution along the notch root produces very similar local shear stress fields for different grain orientation distributions. Earlier, Engel et al. [51] introduced an $E \cdot m$ model in which the product of the orientation-dependent Young's modulus E and Schmid factor m correlates strongly with crack initiation. Further work by Engel et al. [52] using crystal-plasticity simulations for IN-738 LC showed that grain–grain interactions in random or mixed textures can shift plasticity from grains with the highest $E \cdot m$ to nominally "soft" neighboring grains. Acharya et al. [53] have shown that for directionally-solidified and single-crystal nickel-based superalloys, Young's modulus E can be used as an input to account for the effects of grain orientation on fatigue life. Their model predicts an inverse relationship between fatigue life and E, yielding the longest fatigue life for the $\langle 001 \rangle$ orientation – which is consistent with the findings of Li et al. [47] – and the shortest fatigue life for the $\langle 111 \rangle$ orientation. Probabilistic methods, for example, can account for uncertainties in grain orientation. Engel et al. [54] combined polycrystalline finite-element simulations with slip-system-based probabilistic life models for coarse-grained René 80. They showed that differences in grain size and grain orientation distribution between random and textured batches at $850\,^\circ$ C are quantitatively reflected in the predicted LCF life distributions, whereas a purely Weibull-based approach could not capture this microstructure-induced life shift.

2.3. Probabilistic fatigue life modeling

In a probabilistic approach, instead of calculating a fixed deterministic life value N, a life distribution $N(\mathbf{X})$ is quantified. Here, $\mathbf{X}$ is the input property vector that represents the uncertainties [35]. These uncertainties can include material properties, stresses and temperatures, defect sizes and locations. In particular, in the presence of potential defects, non-destructive inspection capabilities and schedules can be included. The non-destructive inspections, such as ultrasonic or X-ray inspections, can be represented by a probability of detection for different defect types and sizes. For further details, see the probabilistic fracture mechanics code DARWIN for aero engines [55] as well as the ProbFM code for heavy-duty energy gas turbines [35,56]. The failure criteria for the individual lives N_{i} of the distribution N can be the same as for a deterministic calculation, including exceeding a critical stress intensity factor K_{C}, or exceeding a critical crack size for crack failure and fatigue crack initiation, respectively. To practically implement this approach, an acceptable risk level needs to be established, and once reached, the critical part needs to be inspected and potentially replaced [35]. One way to do this is to evaluate the cumulative distribution function (CDF) instead of the probability density function (PDF) $N(\mathbf{X})$. In this case, the CDF represents the probability of failure (PoF), and can be compared to an established acceptable PoF. Numerous approaches to probabilistic material modeling exist for different applications, which differ, among other things, in the definition of the failure criteria and the random variables included in the analysis as well as the statistical description of those variables. In the following several examples are presented:

Bussac and Lautridou [57] used a probabilistic model to predict the influence of ceramic inclusions and porosities in powder metallurgy Nickel (Ni)-based superalloys under LCF loading at elevated temperatures. They were able to predict the maximum permissible size of surface inclusions which will provide a specified probability of failure utilizing inclusion size distributions and a harmfulness criterion based on either the penetration depth, or an estimated penetration area of surface flaws assumed to be ideally spherical. However, the criterion is not based on fatigue crack propagation data and does not directly include stresses, strains or temperature. Hence the relative ranking of defect harmfulness is assumed to be independent of the testing conditions. Melis et al. [58] used a probabilistic approach to estimate the design survivability and life of aircraft gas turbine engine compressor disks from a titanium alloy (Ti-6Al-4V) under LCF loading based on Weibull statistics, finite-element analysis and probabilistic material-life properties. Engels et al. [59] proposed a concept for probabilistic blade attachment evaluation of stationary gas turbine steel rotor disks under LCF loading. Their approach considers heterogeneous properties of forging flaws, material properties and nondestructive testing specifications - as discussed in [60] – and assumes a separation of the mechanisms of crack initiation and crack growth. The latter was modeled using Paris' law [61]. Harder et al. [62] use an epidemiological model to assess the fatigue life of a Ni-based superalloy under LCF conditions. They used Coffin-Manson-Basquin [14,15] and Ramberg-Osgood [29] equations with probabilistic Schmid factors to compute crack initiation times. Radaelli et al. [63–65] and Yang et al. [66] investigated fatigue crack nucleation at forging flaws in forged heavy-duty gas turbine rotor steels (e.g., 3.5NiCrMoV). They performed LCF tests on specimens with real forging flaws from scrap rotor disks and used beach-marking to separate the nucleation phase from the subsequent fatigue crack growth phase. Radaelli et al. [63] introduced a probabilistic fracture-mechanics framework that combines nucleation life and crack-growth life via direct Monte Carlo simulation at rotor-disk level. In follow-up work [64,65] they developed and calibrated a local probabilistic LCF-based nucleation model (Weibull statistics with size and notch effects, extended to elevated temperatures). This model uses finite-element analyses of defects idealized as (semi-)ellipsoids and links ultrasonic testing indications, loading, temperature, and defect morphology to the nucleation behavior. Yang et al. [66] proposed a fracture-mechanics-based probabilistic nucleation model that uses the range of the plasticity-corrected stress-intensity factor ΔK_J as crack-driving force. The resulting nucleation-life distribution was integrated into Siemens Energy's probabilistic fracture-mechanics framework ProbFM [56,60]. ProbFM combines ultrasonic testing, defect sizing based on an equivalent circular disk-shaped reflector, statistical conversion from this indication to a true flaw size, direct Monte Carlo simulation, and a weakest-link evaluation to obtain the probability of failure of the component. Mäde et al. [67] use a hazard density approach. Local crack initiation probabilities are calculated from FEM-computed stresses and experimentally calibrated Weibull parameters, and then integrated over the component or specimen surface. This yields a geometry-independent assessment of crack initiation life under LCF loading. The approach shows good agreement for the superalloys IN-939 and René 80 as well as for the steel 26NiCrMoV14-5, across different notched specimen geometries.

Despite various known models, it remains unclear how the morphologically complex casting defects affect fatigue life in MAR-M247 CC depending on their size and shape under LCF loads and high temperatures. Their effect is especially uncertain in the context of a real turbine blade microstructure.

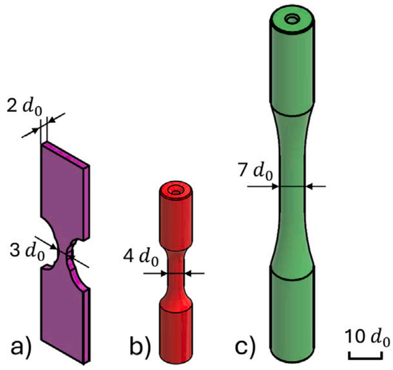

Fig. 2. Geometries of specimens extracted from turbine blades: (a) Flat specimen for thin-walled blade regions, (b) Cylindrical specimen for blade regions with moderate wall thicknesses, (c) Cylindrical specimen for blade regions with large wall thicknesses.

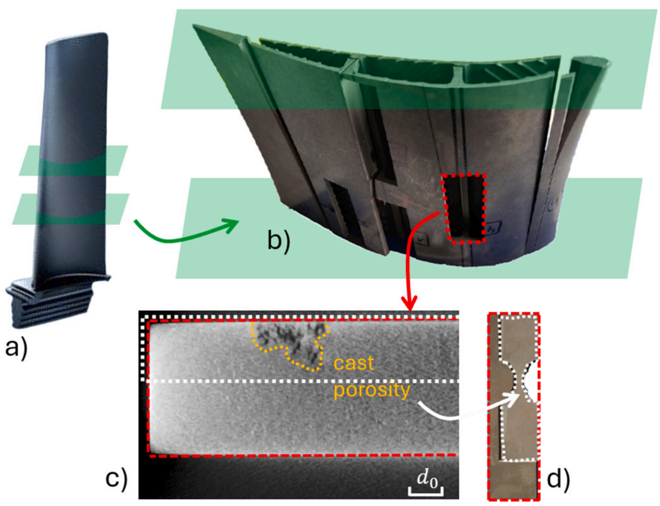

Fig. 3. Extraction strategy for specimens containing cast porosity: (a) CT scan of the entire blade, (b) Pre-segmentation and extraction of specimen blanks, (c) μCT scan of specimen blank, (d) Precise placement of defects in the specimen gauge section.

3. Materials and methods

3.1. Non-destructive testing, specimen design and extraction

Within this work, both defect-free and specimens containing casting defects were extracted from turbine blades. Initially, complete turbine blades were subjected to non-destructive testing using computed tomography (CT). Based on this data, defect-free specimens were extracted from blade regions, where no defect indications were found. Depending on the available wall thickness, either cylindrical or flat specimens were extracted, as shown in Fig. 2. Cylindrical specimens are generally preferred, but their extraction was only possible from the lower blade regions, i.e., near the blade root. Dimensions are given as multiples of the normalization parameter d_0.

For the specimens containing defects, casting defects in a turbine blade were deliberately positioned in the gauge sections of flat specimens. However, it was found that both the resolution of the CT data and the positioning accuracy were insufficient for precise specimen extraction. This issue arises from the size ratios between defects and blades (2:1000), as well as the radiographic properties of the Ni-based superalloy. Additionally, inaccuracies in the necessary overlay of scan

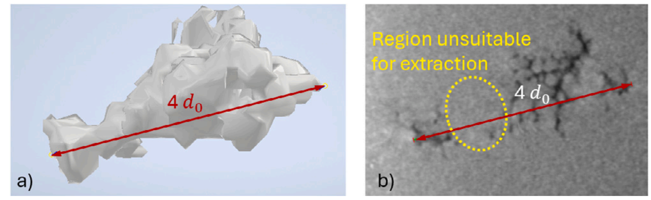

Fig. 4. Comparison of CT results of a casting defect from a turbine blade: (a) Segmented defect from the CT scan of the entire blade, (b) μCT image of the same defect positioned within a specimen blank.

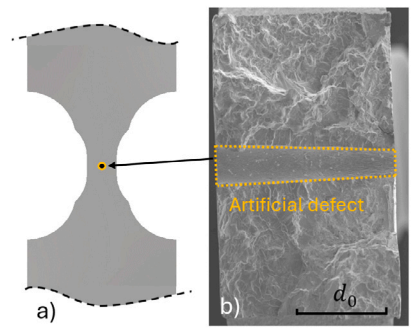

Fig. 5. (a) Schematic representation of the positioning of artificial defects in the gauge section of flat specimens. (b) SEM image of the fracture surface of a flat specimen with an artificial defect introduced by water jet cutting.

results with the CAD data of the blade, as well as manufacturing uncertainties – such as material loss due to cuts during pre-segmentation of the blade – contributed to insufficient positioning accuracy. Since the gauge sections of the flat specimens are small, even minor deviations can result in a failure to position the defect accurately. To address this issue, a multi-step procedure for specimen extraction was developed, which is schematically illustrated in Fig. 3. Based on the initial CT scan, specimen blanks were first extracted at the locations where defects were identified. Each blank was individually adjusted in position, orientation, and size to the respective defect. This was necessary primarily because the wall thicknesses and radii of curvature vary significantly in the blade from one position to the next, and defects vary greatly in size and morphology. The casting defects often consist of finely branched, interdendritic network structures that can only be resolved to a limited extent in a full blade CT scan. Therefore, a μCT scan (i.e., a small-scale high-resolution CT scan) was subsequently performed on each specimen blank. Fig. 4 shows a comparison of images obtained with the different CT scan steps utilized. The μCT scan made a precise extraction possible, as well as determining which regions of the original defect indication were suitable for extraction. Based on the more precise knowledge of defect position and morphology obtained by the μCT, final specimen extraction was performed. Each specimen was individually extracted from a single blank. If necessary, the geometry of the specimen clamping section was individually adjusted, and in some cases, the thickness of the specimen or the width of the specimen gauge section was modified, to make a defect extraction possible. In addition to specimens with casting defects from turbine blades (in the following referred to as "natural" defects), specimens with "artificial" defects were also manufactured and tested. For this purpose, originally defect-free specimens from a turbine blade were modified with small holes in the gauge section, as indicated in Fig. 5(a). Artificial defects were introduced using either water jet cutting – as depicted in Fig. 5(b) –, drilling, or EDM die sinking. Artificial defects were varied in size, i.e., diameter and depth. The artificial defects are intended to expand the database of natural defects and represent a significantly more cost-effective alternative.

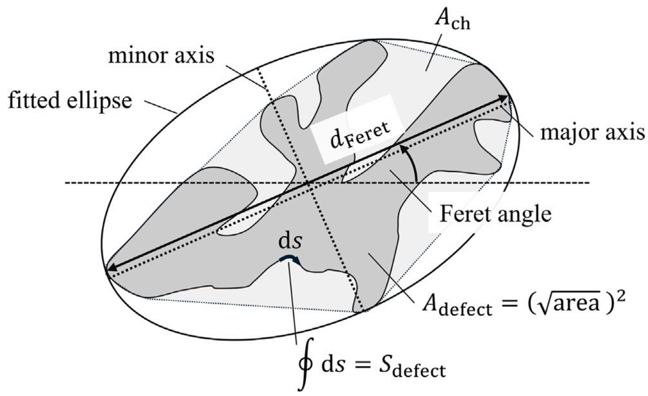

Fig. 6. Schematic representation of investigated defect parameters.

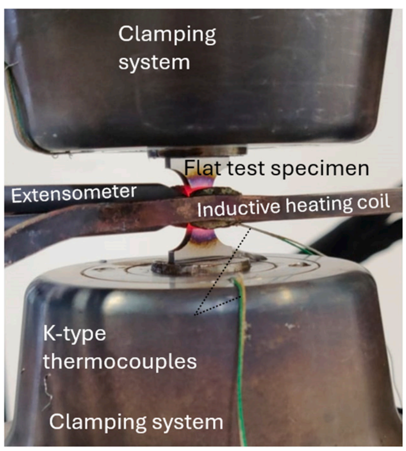

Fig. 7. Test setup for high-temperature tests under fully reversed low-cycle fatigue (LCF) loading on flat specimens from turbine blade material.

3.2. Defect parameterization

Defects are parameterized based on specimen fracture surfaces, as schematically depicted in Fig. 6. Two parameters for defect size ($\sqrt{\text{area}}$ and d_{Feret}), one parameter for defect orientation (Feret angle), and three parameters for defect shape (circularity, aspect ratio and solidity) are studied. The parameter $\sqrt{\text{area}}$, following Murakami's [41] notation, represents the square root of the defect area on the specimen fracture surface. The defect area itself is here also denoted as A_{defect}. d_{Feret} is the maximum Feret diameter of the defect on the fracture surface. The Feret angle denotes the angle of d_{Feret} with respect to the horizontal, which corresponds to the short side of the flat specimens. For reasons of symmetry, angles are limited to values between 0 ° and 180 °. The solidity γ is a measure for the compactness of the defect on the fracture surface and is defined as:

$$\gamma = \frac{A_{\text{defect}}}{A_{\text{ch}}}, \tag{13}$$

where A_{ch} is the area of the convex hull around the defect contour on the fracture surface. The circularity ζ describes how closely the shape of the defect contour on the fracture surface resembles that of an ideal circle. The parameter is defined as follows:

$$\zeta = 4\pi \frac{A_{\text{defect}}}{S^2_{\text{defect}}}, \tag{14}$$

where S_{defect} is the perimeter i.e., the length of the defect contour on the specimen fracture surface. The aspect ratio is defined by the ratio

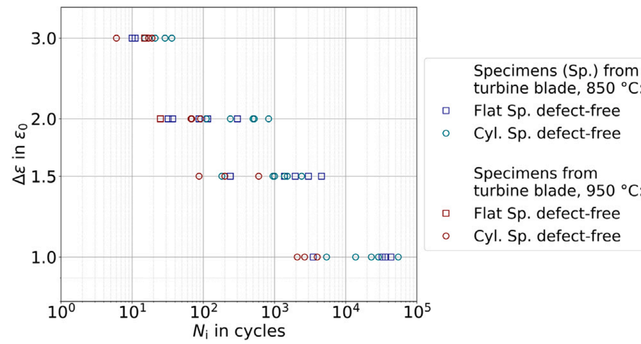

Fig. 8. Strain-life diagram of the conducted LCF tests on defect-free turbine blade material.

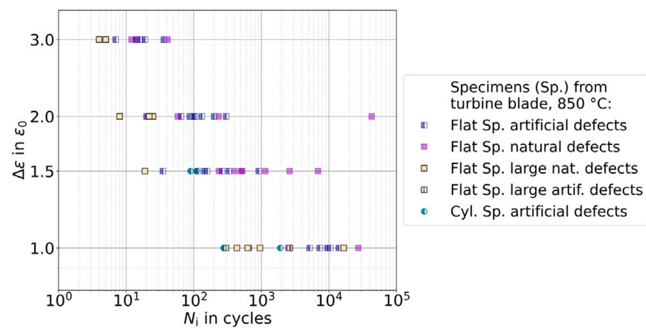

Fig. 9. Strain-life diagram of the conducted LCF tests on turbine blade material containing defects.

of the major and minor axis of a fitted ellipse around the defect:

$$\text{aspect ratio} = \frac{\text{major axis}}{\text{minor axis}}. \tag{15}$$

4. Experimental work

4.1. Uniaxial high temperature LCF tests

LCF-tests were conducted based on ISO Standard 12106 [68] using a universal testing machine Instron 8862 with an electromechanical drive. The testing system was calibrated according to DIN EN ISO 7500-1 [69]. The tests were primarily conducted at 850 °C under strain-controlled conditions with a strain ratio of $R_\varepsilon = -1$ and a strain rate of 10^{-3} s^{-1} (triangular waveform). Additionally, tests were conducted at 950 °C. A high-temperature extensometer Epsilon 3648, calibrated according to DIN EN ISO 9513 [70], was used for strain measurement. The test setup used is shown in Fig. 7. The setup allowed testing of specimens from various blade positions, including those with thin wall thicknesses, such as near the blade tip and at the trailing edge of the blade. Figs. 8 and 9 show the results of the conducted high-temperature tests under LCF loading as strain-life (ε-N) diagrams for defect-free specimens and specimens containing defects, respectively. The experimental number of cycles to initiation of a (technical sized) crack N_i was evaluated based on a stiffness drop criterion, which approximately corresponds to a load drop of 20%.

A considerable scatter is observed for both defect-free specimens and specimens containing defects. In Fig. 9, one outlier is observed at the second highest load level. Large defects mostly seem to result in small N_i.

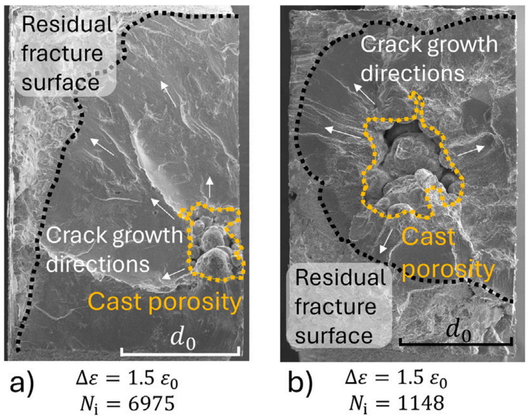

Fig. 10. SEM images of specimen fracture surfaces with natural defects. Defect in (a) is smaller than defect in (b).

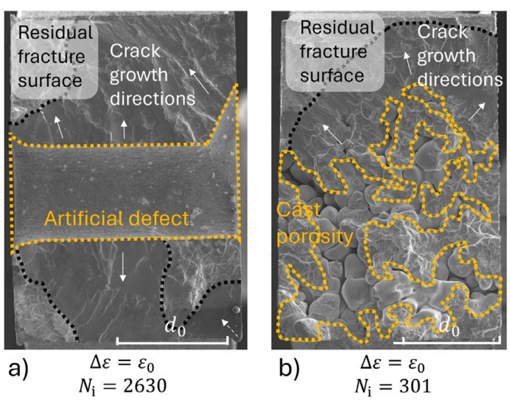

Fig. 11. SEM images of specimen fracture surfaces: (a) artificial defect, (b) natural defect - both large compared to defects in Fig. 10.

4.2. Fractography

The fracture surfaces of the LCF specimens were examined using a Hitachi S-3400N II scanning electron microscope (SEM) from Hitachi High Technologies Europe GmbH using the integrated PC-SEM software. Based on the SEM images, parameters for characterizing defect size, shape and orientation were evaluated using the ImageJ software Fiji. Fig. 10 shows examples of SEM images of flat specimen fracture surfaces. Defects were characterized based on the outlines highlighted in orange. Fig. 11 depicts examples for defects that are large compared to the specimen dimensions, including an artificially introduced defect. In almost all cases where a defect was present in a specimen, the fatigue crack initiated at this defect.

4.3. Investigation of microstructure influence on test and material parameters

The microstructure was investigated using an EBSD Velocity Pro camera from EDAX Inc. on a Zeiss Sigma300 SEM from Carl Zeiss Microscopy Deutschland GmbH, focusing on grain size and orientation. The data was recorded with the APEX™ EBSD software from EDAX Inc. and analyzed with the OIM Analysis™8.6 software from EDAX Inc.. The specimens for EBSD measurements were prepared as follows: they were first ground using SiC abrasive paper with 180 and 500 grit at an applied load of 25–30 N. This was followed by polishing with diamond suspensions with particle sizes of 9 μm and 3 μm at 30 N for 8 min and 6 min, respectively. Final polishing was carried out using an oxide polishing suspension of colloidal SiO_2 with a particle size of 0.1 μm at 20 N for 5 min. The EBSD montage scans were recorded with a voltage of 20 kV, an aperture of 120 μm, and a step size of 5 μm. Both tested LCF specimens and untested specimen plates (15 mm × 22 mm × 2 mm) extracted from turbine blades were examined. The results of the EBSD analyses show significant differences in grain size distributions among the various turbine blade regions, as shown in Fig. 12. Fig. 12 highlights the mean grain size in terms of a grain diameter $\bar{d}_\mathrm{grain}$ and the respective standard deviation σ_SD for a multitude of extraction positions. It was found that in the lower part of the blade grains are larger and more variable than in the upper part. These observations correlate with the radially decreasing wall thickness of the turbine blade. However, a variation of grain size distribution independent of the radial position was also observed, which is related to the complex cross-sectional geometry of the blade. For the examined LCF specimens, both intergranular and transgranular crack growth (e.g., Fig. 13) were observed.

One material parameter for which a large scatter was observed in the experiments is Young's modulus E. Fig. 14 depicts the values found for E during tests on defect-free specimens at 850 °C by evaluating the stress–strain hysteresis present at half of the specimen lifetime. Extreme values for E can be attributed to the anisotropy of the nickel grains and the fact that in some flat specimens only a few large grains were present in the gauge section, as is the case for the specimen shown in Fig. 13. For context, values for nickel single crystals at 850 °C from [53] are also depicted in Fig. 14. The experimentally observed values for E lie within the span between values of the $\langle 001\rangle$ and $\langle 111\rangle$ orientation of a nickel single crystal. As described in Section 4.1, tests were conducted strain controlled with a strain ratio $R_\varepsilon = -1$. However, due to grain-orientation-dependent asymmetries in the deformation behavior, different stress ratios R_σ occurred in the tests conducted. Although R_σ technically is a load parameter, it is presumed that in the present tests for a given specimen geometry and a constant R_ε, R_σ only depends on the microstructure and can therefore be treated similarly to a material parameter. Fig. 15 depicts the experimentally obtained values for E and R_σ. The observed scatter in R_σ is more pronounced for flat specimens, than for round specimens. Although also rooted in the microstructure, the variation observed in R_σ seems to be independent from the scatter found in E as no clear correlation is visible in Fig. 15. This is confirmed quantitatively by Spearman's rank correlation coefficient ρ [71]. It ranges from −1 (strong negative) to 1 (strong positive correlation). The obtained value $\rho = -0.11$ is close to zero, indicating no monotonic correlation between E and R_σ.

5. Fatigue life model for the evaluation of casting defects

5.1. Deterministic model

The suggested deterministic approach models the growth of short fatigue cracks and is based on the cyclic crack tip opening displacement as described by Eqs. (1)–(12). Additionally, an El Haddad-type [72] contribution to the crack length l^* and a cyclic crack tip opening threshold $\Delta CTOD_\mathrm{th}$ as described in [73], are added:

$$\frac{\mathrm{d}a}{\mathrm{d}N} = \beta\left(d_{\mathrm{n}'}\frac{Z_\mathrm{D}}{\sigma_\mathrm{cy}}\left(a + l^*\right) - \Delta CTOD_\mathrm{th}\right)^B. \tag{16}$$

$\Delta CTOD_\mathrm{th}$ is calculated using Eqs. (2) and (5), assuming that the plastic strain range in the threshold region is approximately zero:

$$Z_\mathrm{D,th} \approx 1.45\frac{(\Delta\sigma_\mathrm{eff,th})^2}{E}, \tag{17}$$

where $\Delta\sigma_\mathrm{eff,th}$ is determined according to Eq. (6) with $\Delta\sigma_\mathrm{th}$ as an input instead of cyclic load parameters. $\Delta\sigma_\mathrm{th}$ is the fatigue limit in terms of a stress range for a defect of size a_0 and is used to account for the effect of defects in the threshold regime. The following El Haddad-type [72] relation is used:

$$\Delta\sigma_\mathrm{th} = \frac{\Delta K_\mathrm{th}}{Y\sqrt{\pi\left(a_0 + l^*\right)}}. \tag{18}$$

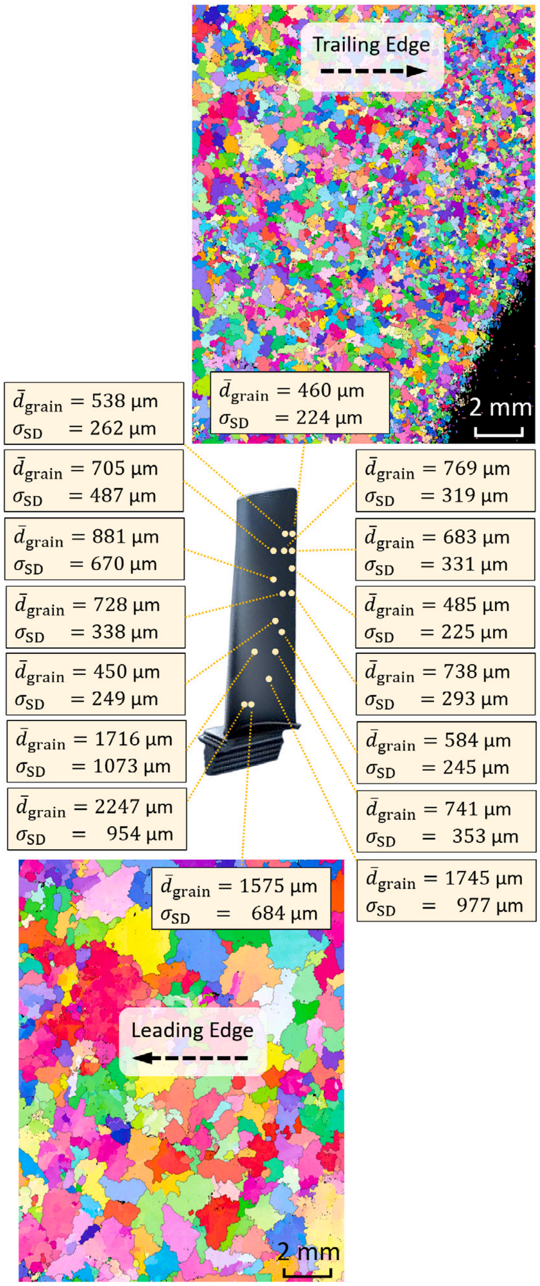

Fig. 12. Mean grain size in terms of average grain diameter $\bar{d}_{grain}$ and the respective standard deviation σ_{SD} for different extraction positions in a cast turbine blade.

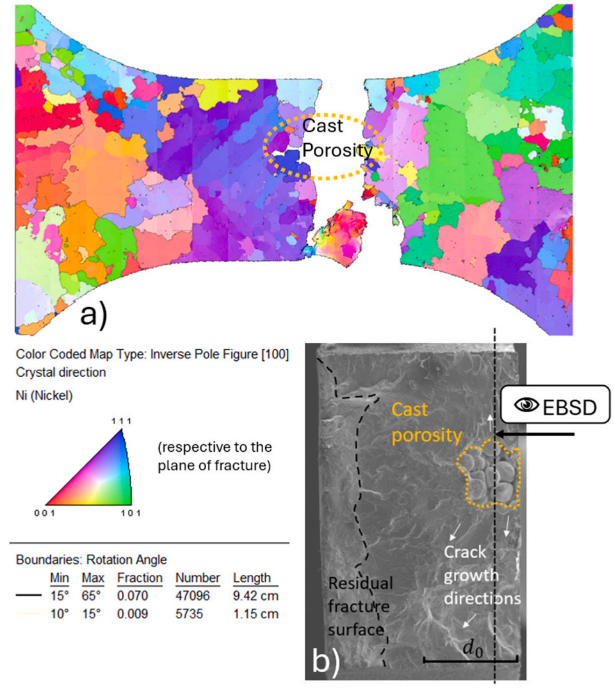

Fig. 13. (a) EBSD image of a flat specimen after testing that contains cast porosity, (b) SEM image of the corresponding fracture surface, highlighting the plane of the EBSD measurement [12].

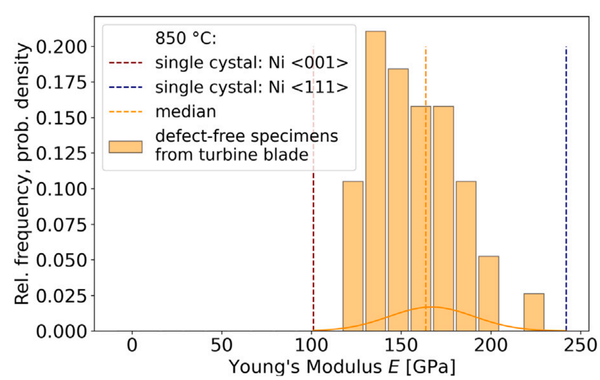

Fig. 14. Experimental distribution of Young's Modulus in defect-free specimens tested at 850 °C in the context of values for nickel single crystals from [53].

Here, ΔK_{th} is the fatigue threshold in terms of a stress intensity factor, which can be determined from fatigue threshold tests. Y is a geometry function. For a short penny-shaped crack $Y = 2/\pi$ and for a small semi-circular surface crack Riedel [33] suggested the simplified solution $Y = 1.12 \cdot 2/\pi$. The El Haddad-type parameter l^* was fitted to the experimental data. The obtained value inserted into Eq. (18) yields values for $\Delta\sigma_{th}$ that agree with the trend of a defect dependent fatigue limit observed in the Data of Šmíd [10] for pre-cast MAR-M247 specimens tested at 800 °C in the HCF regime.

Finally, an analytic expression for the lifetime can be found by integrating Eq. (16) from an initial defect size a_0 to a final crack length a_f [73]:

$$N_f = \frac{\left(d_{n'}\frac{Z_D}{\sigma_{cy}}\left(a_f + l^*\right) - \Delta CTOD_{th}\right)^{1-B}}{(1-B)\, d_{n'}\frac{Z_D}{\sigma_{cy}}\beta} - \frac{\left(d_{n'}\frac{Z_D}{\sigma_{cy}}\left(a_0 + l^*\right) - \Delta CTOD_{th}\right)^{1-B}}{(1-B)\, d_{n'}\frac{Z_D}{\sigma_{cy}}\beta}. \quad (19)$$

While Schackert et al. [73] assumed $a_0 = 0$ mm and $a_f = 1$ mm in their model for a defect free material, here, $a_0 = d_{Feret}/2$ is assumed to implement a defect size dependence. This model assumption is justified by findings presented in Section 6. The model therefore represents each defect as an idealized equivalent initial crack. For defect-free specimens $d_{Feret} = 0$ is used. Furthermore, it is assumed that the

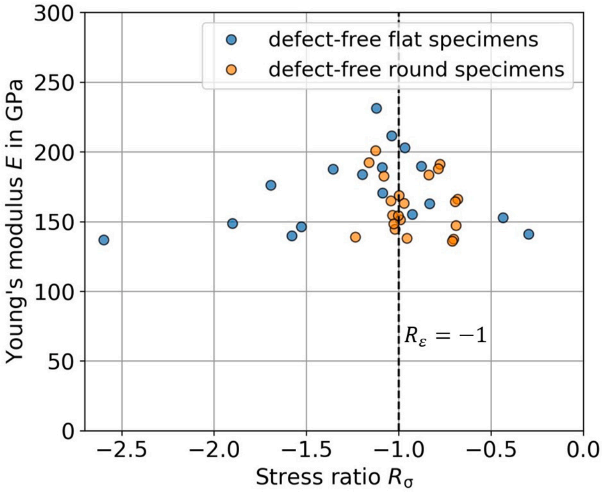

Fig. 15. Experimentally observed scatter of the microstructure-dependent parameters E and R_σ.

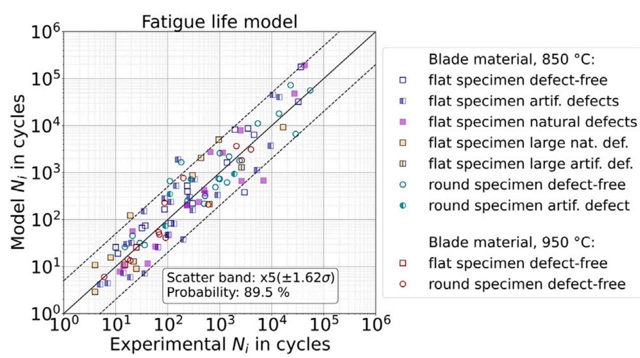

Fig. 16. Deterministic model assessment of LCF lifetime in MAR-M247 at high temperatures considering the effect of casting defects.

experimentally observed load drop, caused by the growing crack, can be approximated by the reduction of the load-bearing cross-sectional area of the specimen gauge section. Hence, the final crack length is determined by solving Eq. (20) for a_f, individually for each specimen geometry and each initial defect size. The target value 0.8 corresponds to a load drop of 20%:

$$0.8 = \frac{A_\mathrm{s} - A_\mathrm{crack}(a_\mathrm{f})}{A_\mathrm{s} - A_\mathrm{crack}(a_0 = d_\mathrm{Feret}/2)}, \tag{20}$$

where A_s is the cross section area of the undamaged specimen. In accordance with the crack geometry underlying the derivation of Z_D in Eq. (5), a semi-circular crack area $A_\mathrm{crack}(a) = \pi a^2/2$ is assumed.

5.2. Results for experimental LCF data

The parameters E, $\Delta\sigma_\mathrm{eff}$, $\Delta\sigma$ and $\Delta\varepsilon_\mathrm{pl}$ in Eq. (5), as well as R_σ in Eq. (7), are determined individually for each test from the experimental stress–strain-hysteresis loops at half of each specimen's lifetime. For σ_cy and n', values from [22] are used depending on the temperature. Fig. 16 depicts the model assessment of the LCF lifetime N_i against the experimental N_i. For 850 °C and 950 °C the same model parameters are used. The temperature dependence is accounted for through the material parameters.

For different specimen geometries, different high temperatures, defect-free specimens and specimens containing defects, as well as for different defect types (i.e., natural and artificial) and a multitude of different defect sizes, the model is able to assess the lifetime within

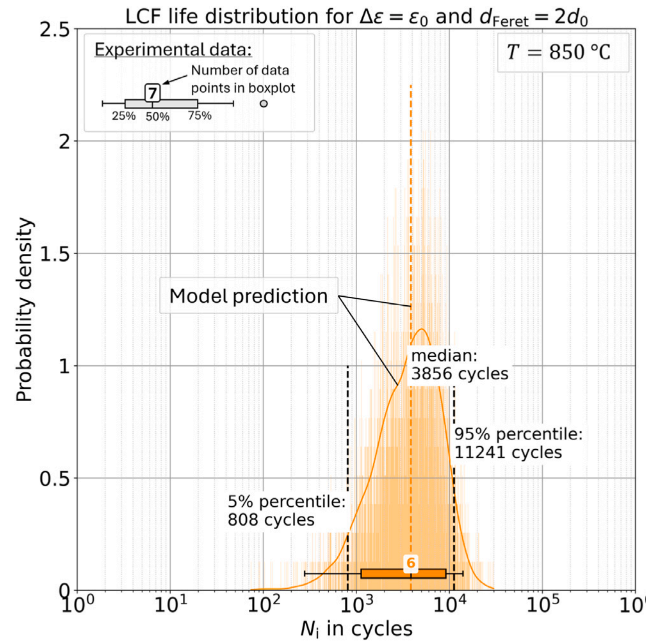

Fig. 17. Probabilistic model assessment of LCF lifetime in MAR-M247 CC at 850 °C for a constant load and defect size.

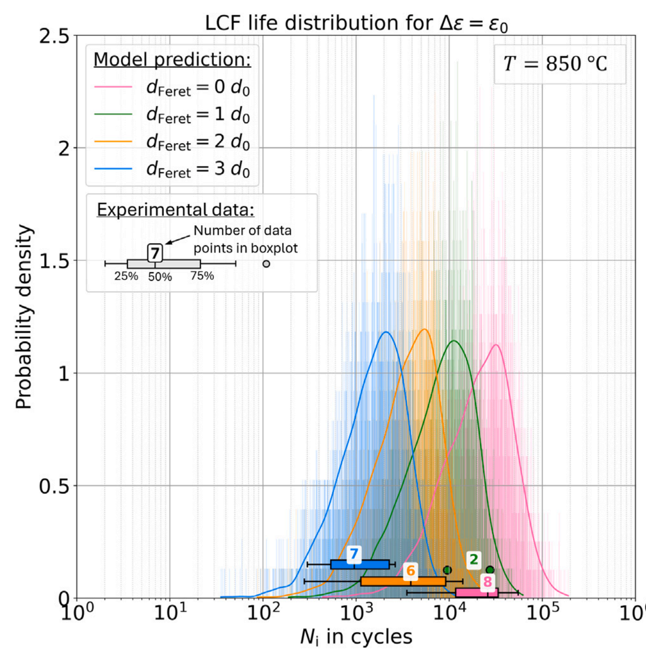

Fig. 18. Probabilistic model assessment of LCF lifetime in MAR-M247 CC at 850 °C for a constant load and different defect sizes.

a scatter band of ± factor five. In Fig. 16, particularly large defects (compared to the specimen dimensions) are highlighted separately in yellow.

5.3. Probabilistic model

The probabilistic model is based on the deterministic model equations given in Section 5.1, but additionally takes into account the statistical scatter of the material to assess a fatigue life distribution for a given load and defect size. This requires parameters that are suitable for reflecting the scatter in fatigue life observed experimentally. By applying the deterministic model, it was shown that the experimental lifetimes can be described well for different loads and defect sizes, assuming a constant cyclic yield stress σ_{cy} and a constant strain hardening exponent n', if the parameters Young's modulus E and stress ratio R_σ are considered individually for each specimen. For this reason, and based on Sections 2.2 and 4.3, E and R_σ are used in the probabilistic model as parameters to describe the statistical scatter of the material observed in the experimental investigations. A number of different theoretical distribution functions were fitted to the experimentally determined empirical distribution of the parameters E (Fig. 14) and R_σ (Fig. 15) of defect-free specimens. The best fitting distribution was identified using a Kolmogorov–Smirnov test [74,75], respectively. For E, a Weibull distribution was fitted to the empirical distribution. The theoretical function however, was restricted to the physical limits visible in Fig. 14 for both ends of the distribution. A t-distribution best described the experimental data of R_σ, which was additionally limited to only negative values for R_σ. By means of a Monte Carlo simulation, random samples are taken from the theoretical distributions for E and R_σ and a fatigue life is determined using Eq. (19) for each sampled pair of E and R_σ. This ultimately yields a fatigue life distribution provided that the sample size is large enough. For a given strain range $\Delta\varepsilon$, stresses are calculated using a cyclic Ramberg-Osgood law [29].

Fig. 17 depicts the model's LCF life assessment for defect size $d_{\text{Feret}} = 2d_0$ and strain range $\Delta\varepsilon = \varepsilon_0$. The assessment is given in terms of a probability density resulting from the relative frequency of a Monte Carlo simulation with a sample size of 5000, which is shown as a histogram in Fig. 17. Note that the probability density refers to $\log N_i$ due to the logarithmically scaled abscissa. The probability of failure (PoF) can be determined by integrating the probability density up to a desired target life. For comparison, experimental results for this load, corresponding to a defect size of approximately $d_{\text{Feret}} = 2d_0$, are shown as a box plot. The model reproduces the experimental median very well. All experimental data points fall within the modeled scatter range. The tendency toward a slightly left-skewed distribution is also captured by the model. The Fig. 18 and Fig. 19 illustrate the model's capability to take different defect sizes and strain ranges into account, respectively.

6. Influence of defects on LCF lifetime

6.1. Identification of independent defect parameters

The influence of defects on the fatigue life is characterized based on the parameters described in Section 3.2. Firstly, a correlation analysis is conducted based on the rank correlation coefficient suggested by Spearman [71], to assess the relationship between the defect parameters investigated. Values of the rank correlation coefficient range from −1 to 1. A value close to 1 indicates a strong positive correlation, a value close to −1 indicates a strong negative correlation, and a value close to 0 indicates no correlation. The full correlation matrix is depicted in Fig. 20. Based on this analysis, the parameter defect circularity is not investigated further, as it strongly correlates with the defect solidity. Furthermore, a positive correlation of the two investigated defect size parameters $\sqrt{\text{area}}$ and d_{Feret} is observed. In the model, d_{Feret} is used to describe the size of the defects, although $\sqrt{\text{area}}$ would be equally suitable in this case. The correlation matrix for the remaining defect parameters is shown in Fig. 21. Here, also the distribution of each remaining defect parameter, as well as the scatter plots of the remaining parameters against each other, are visualized. In addition, for each combination of remaining defect parameters, p-values were computed and compared to a conventional level of significance $\alpha = 0.05$ under the null hypothesis that there is no monotonic relationship between the two parameters analyzed. Computed p-values had an average of 0.47, not dropping below 0.14. Since $0.14 > \alpha = 0.05$, there is insufficient evidence to reject the null hypothesis. This should not be interpreted as a probability that the null hypothesis is true [76,77]. In combination with the previous results, however, further investigations do not appear justified and it is assumed that the remaining defect parameters are independent.

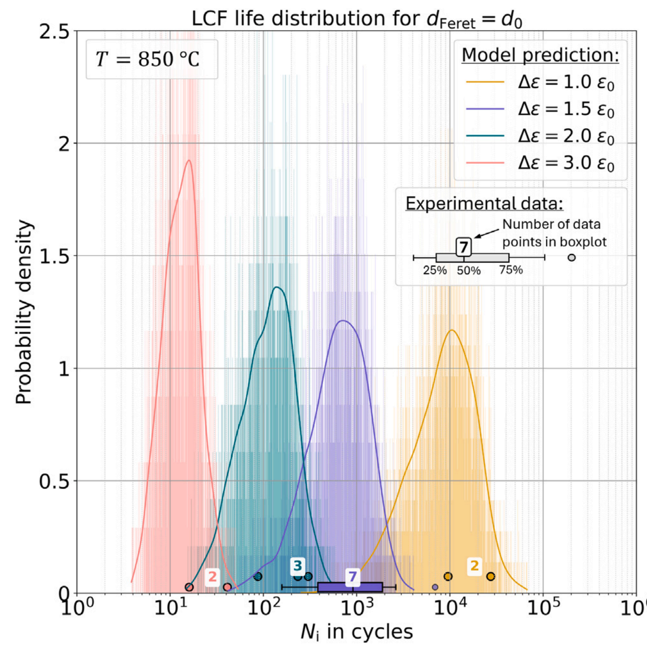

Fig. 19. Probabilistic model assessment of LCF lifetime in MAR-M247 CC at 850 °C for a constant defect size and different loads.

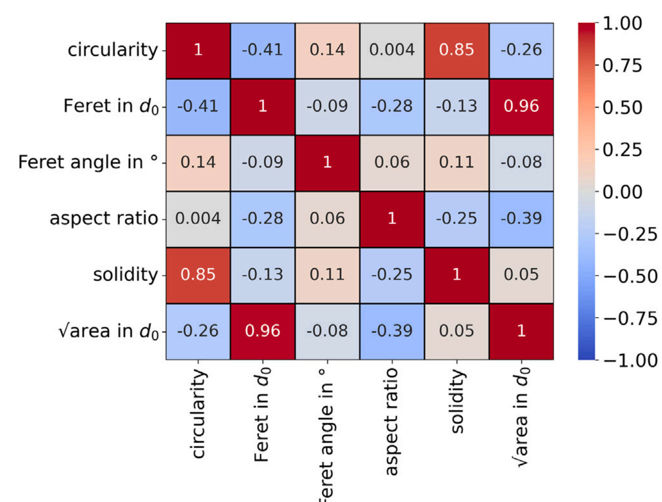

Fig. 20. Spearman correlation analysis of all defect parameters investigated.

6.2. Defect parameter influence on LCF lifetime

6.2.1. Defect size

First, the influence of defect size – characterized by the parameter d_{Feret} – is investigated. Fig. 22 shows the experimental lifetime obtained in LCF-tests on turbine blade material at 850 °C against the respective values of d_{Feret} for each specimen. Four different strain ranges were tested, which are differentiated by color in Fig. 22. Defect-free specimens are depicted with $d_{\text{Feret}} = 0$ and with open symbols. For tests on defect-free specimens, box plots are given, where n is the number of tests conducted. Square symbols indicate flat specimens, while circular symbols indicate round specimens. Filled symbols denote specimens containing natural defects (i.e., casting defects extracted

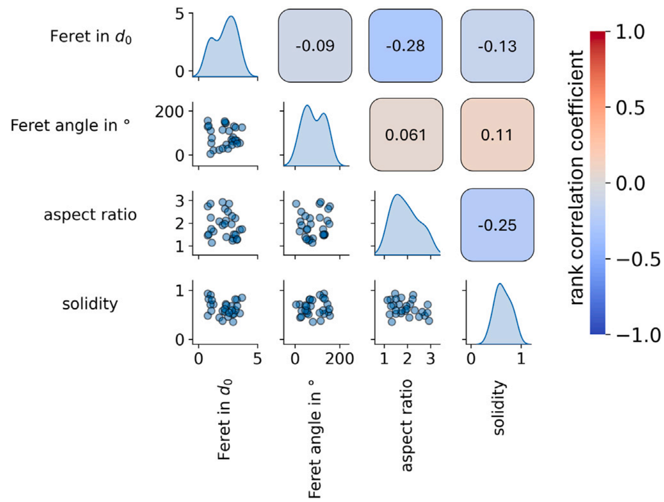

Fig. 21. Spearman correlation analysis of independent defect parameters investigated.

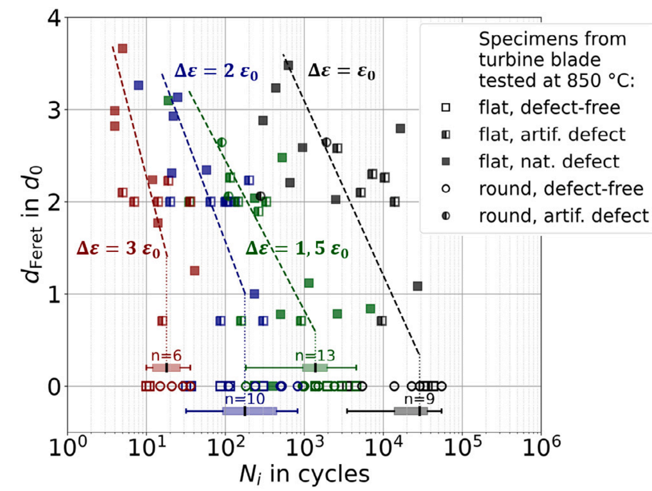

Fig. 22. Influence of defect size, characterized by d_{Feret}, on the LCF lifetime at 850 °C.

from turbine blades). Half-filled symbols mark specimens where defects were introduced artificially. The specimens with artificial defects fit in well with the trend of the natural defects. In Fig. 22, a clear dependence of fatigue life on defect size, characterized by the Feret diameter on the fracture surface, can be observed across all load levels. A linear fit to the logarithm of the fatigue life shows the observed trend for each load level, respectively (dashed lines). The influence of d_{Feret} on N_{i} seems to be slightly more pronounced at small loads ($\Delta\varepsilon = \varepsilon_0$ and $\Delta\varepsilon = 1.5\,\varepsilon_0$). Furthermore, for small values of d_{Feret} the influence on N_{i} seems to be limited. It is observed that the larger the loading, the larger the defect size required to significantly reduce the lifetime. In other words, the material seems to be more sensitive to small defects under small loads. In Fig. 22, this is highlighted by extending the medians of the defect-free tests (dotted lines) up to the point, where they intersect the fit of the defective data (dashed lines). With the exception of two outliers, the scatter of the defective data can be explained by shifting the median of a Weibull distribution function fitted to the defect-free series along the dotted and dashed lines for each strain range, respectively. This indicates that the remaining scatter in fatigue life visible in Fig. 22, which is observed after taking the defect size into account, mainly is not caused by defects.

6.2.2. *Defect shape and orientation*

The strong correlation between fatigue lives and defect size shown in Section 6.2.1 suggests a weaker correlation for the remaining defect parameters. To analyze this further, the deterministic LCF lifetime model (description in Section 5.1) is used as it is able to consider the influence of the defect size.

Figs. 23–25 depict the distribution of the respective defect parameter within the LCF test data assessed by the suggested deterministic model. In the plot of the model N_{i} versus the experimental N_{i}, a systematic pattern in the distribution within the scatter band should be recognizable for the investigated defect parameters – in the case that the corresponding parameter has a significant influence on the fatigue life. For example, fatigue lives of defects with low solidity could be systematically assessed too short, because a certain amount of additional cycles is needed for the formation of a uniform crack front, compared to defects which exhibit a high solidity. Findings from Varfolomeev et al. [78] on forging flaw clusters in a rotor steel suggest that such a relationship may exist. However, such an observation can be made neither for the defect aspect ratio (Fig. 23), nor for the defect solidity (Fig. 24), nor for the Feret angle (Fig. 25). In all cases, the values of the investigated defect parameter lie arbitrarily in the scatter band. It is therefore concluded that the investigated shape and orientation parameters have no significant influence on the fatigue life.

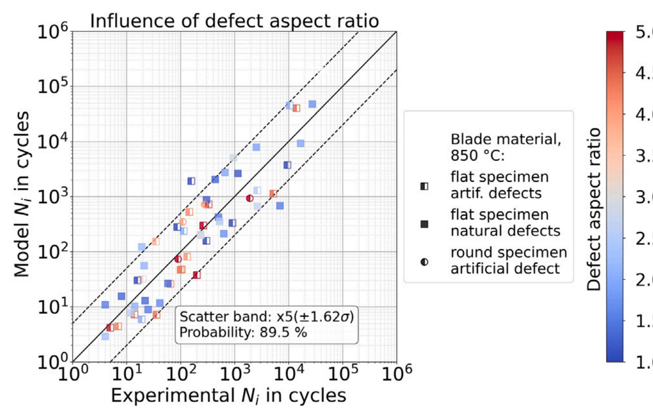

Fig. 23. Color coded defect aspect ratio for model N_{i} vs experimental N_{i} plot.

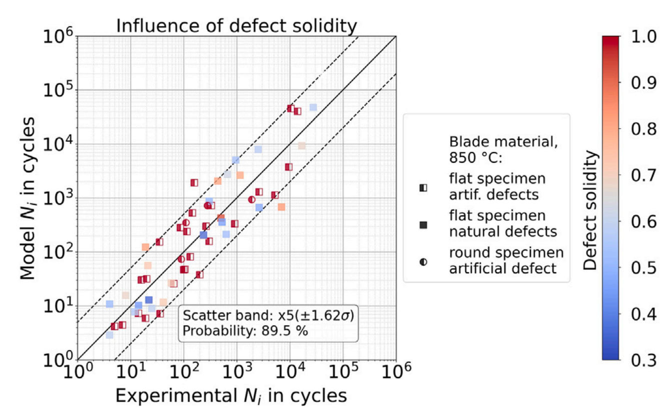

Fig. 24. Color coded defect solidity for model N_{i} vs experimental N_{i} plot.

7. Discussion

7.1. *Experimental findings*

The large scatter observed in the experimental lifetimes (Fig. 8) is due, among other factors, to the influence of defects and microstructural differences between the samples. The outlier at the second-highest

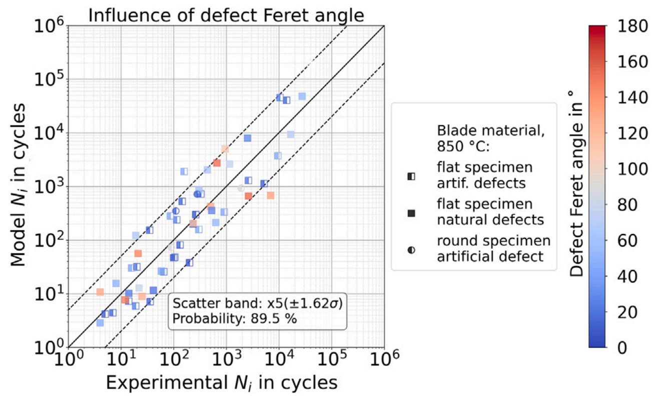

Fig. 25. Color coded defect Feret angle for model N_i vs experimental N_i plot.

load level represents a case in which various factors combine to favor a long fatigue life. First, the specimen has a comparatively low Young's modulus E. This reduces the stress amplitudes in strain-controlled tests relative to materials with average E. In addition, the specific microstructure of this specimen leads to a stress ratio of only $R_\sigma \approx -1.5$ during testing (strain ratio $R_\varepsilon = -1$). The resulting low tensile stresses further promote long fatigue life. The scatter of E and R_σ is shown in Fig. 15. Third, in this exceptional case the fatigue crack initiated at the specimen surface rather than at an existing defect. However, the outlier can be assessed appropriately regarding N_i by using specimen-specific values for E, R_σ and suitable defect parameters (i.e., $d_\mathrm{Feret} = 0$). This is shown in Fig. 16, where the outlier falls into the scatter band.

In this work, the physical differences between artificial and natural defects (e.g., shape, surface roughness, residual stresses) do not appear to have a major influence on fatigue life compared to the large scatter originating from the microstructure. Nevertheless, this may be an interesting topic for future investigations. An influence of the type of crack propagation (intergranular or transgranular) is assumed, but could not be investigated in sufficient detail within the scope of this work. The analysis of grain size distributions revealed that the grain sizes in the component are of a similar magnitude as the size of the defects. It is possible that the formation of cracks in the case of small defects is dominated by the microstructure. This may indicate why small defects do not significantly affect fatigue life - as observed in Section 6 (Fig. 22). However, a much more extensive investigation would be required to clarify this question conclusively. Still, the present results indicate that grain orientation and size play a significant role in fatigue life. This confirms the approach of the probabilistic model to describe lifetime scatter through the scattering of material parameters that depend on grain orientations and sizes.

It is emphasized that the correlations identified between the investigated defect parameters do not necessarily represent universally valid relationships. They are influenced by the chosen specimen geometry and the boundary conditions resulting from the specimen extraction performed in this study. Correlations may differ in the component or under alternative boundary conditions. Nevertheless, the results presented provide indications of relevance and influence of different defect characteristics, which can support the assessment of components.

7.2. Assessment of finite defects and cracks

Some of the defects and cracks in this work are large in proportion to the cross-section of the flat specimen. The application of the cyclic J-integral or Z_D-based fracture mechanical approximation solution must be critically reviewed, as it was derived for a small crack in a semi-infinite space [33]. Using an approximate solution by He and Hutchinson [79] for the plastic limit case, the J-integral for a circular crack in an infinite medium under mode I loading can be written as follows:

$$J_\mathrm{pl} = \frac{6}{\pi} \frac{\sigma \varepsilon_\mathrm{pl}}{\sqrt{1+3n'}} a. \tag{21}$$

Within Eq. (21), the term $\frac{\sigma\varepsilon_\mathrm{pl}}{\sqrt{1+3n'}}$ can be approximated using the plastic strain energy density w' for power-law hardening material behavior:

$$w' = \int \sigma \, \mathrm{d}\varepsilon_\mathrm{pl} = \frac{1}{n'+1} \sigma \varepsilon_\mathrm{pl}, \tag{22}$$

because the difference between $1/(n'+1)$ and the factor $1/\sqrt{1+3n'}$ leads to a maximum difference of approximately 6% for $n' \in [0,1]$. Hence, J_pl can be written as

$$J_\mathrm{pl} = \frac{6}{\pi} \int \sigma \, \mathrm{d}\varepsilon_\mathrm{pl} \, a. \tag{23}$$

An unknown correction factor $f(a,w)$ – i.e., a geometry function – can be added to Eq. (23) to account for the crack geometry in relation to the specimen thickness w. For the fully plastic case, including $f(a,w)$ yields:

$$J_\mathrm{pl} = f(a,w) \frac{6}{\pi} \int \sigma \, \mathrm{d}\varepsilon_\mathrm{pl} \, a. \tag{24}$$

An alternative definition of J was formulated by Rice et al. [80], based on the area under the force–displacement curve. Schweizer [21] adapted this approach to generate a geometry function Y_area for the corner-crack specimen containing a quarter-circular crack in a quadratic cross-section and used the engineering stress σ instead of the force. Additionally, it is assumed, that in the fully plastic case the increment of the displacement can be approximated by $\mathrm{d}u \approx \mathrm{d}\varepsilon_\mathrm{pl} l_0$:

$$J_\mathrm{pl} = Y_\mathrm{area}(a,w) \int \sigma \, \mathrm{d}\varepsilon_\mathrm{pl} \, l_0, \tag{25}$$

where $Y_\mathrm{area}(a,w)$ is another geometry-dependent parameter which depends on the normalized crack length a/w and the location of the displacement measurement (in the underlying simulations $l_0/w = 10/8$). l_0 denotes the gauge length of the extensometer. The explicit expression for Y_area is given by a fourth-order polynomial function [21]:

$$\begin{aligned} Y_\mathrm{area}(a,w) = & -0.007 + 2.15064(a/w) + 1.088(a/w)^2 \\ & - 6.05696(a/w)^3 + 4.096(a/w)^4. \end{aligned} \tag{26}$$

Equating Eqs. (24) and (25) yields:

$$f(a,w) \frac{6}{\pi} \int \sigma \, \mathrm{d}\varepsilon_\mathrm{pl} \, a = Y_\mathrm{area}(a,w) \int \sigma \, \mathrm{d}\varepsilon_\mathrm{pl} \, l_0, \tag{27}$$

which can be solved for $f(a,w)$:

$$f(a,w) = Y_\mathrm{area}(a,w) \frac{\pi}{6} \frac{l_0}{a}. \tag{28}$$

Y_area is nearly independent of the strain hardening exponent and the applied load. With the polynomial solution for $Y_\mathrm{area}(a,w)$ and Eq. (28), $f(a/w)$ can be estimated and compared to the geometry factor of the Z_D-type solution, which is 1.12^2. Fig. 26 shows the comparison between $f(a,w)$ and the geometry factor used within Z_D. For $a/w < 0.375$, Z_D underestimates the crack-length dependence of the geometry factor by up to 12%. For $a/w > 0.375$, Z_D overestimates the geometry factor. At $a/w = 0.5$, the deviation is -12% compared to geometry factor used in the model. For a defect-free flat specimen, the crack driving force is initially underestimated and later overestimated by the model (blue area in Fig. 26). The use of the geometry factor 1.12^2 provides a reasonable approximation for the defect-free case, as the deviations are approximately balanced across the crack extension up to the final crack length, which in this case is $a_\mathrm{f}/w \approx 0.5$. However, the overestimation increases with further increasing a/w up to a maximum of −37% at $a/w = 0.88$. Hence, the model based on Z_D overestimates the crack driving force in terms of ΔJ for defects and cracks that are large compared to the specimen dimensions (beige area in Fig. 26).

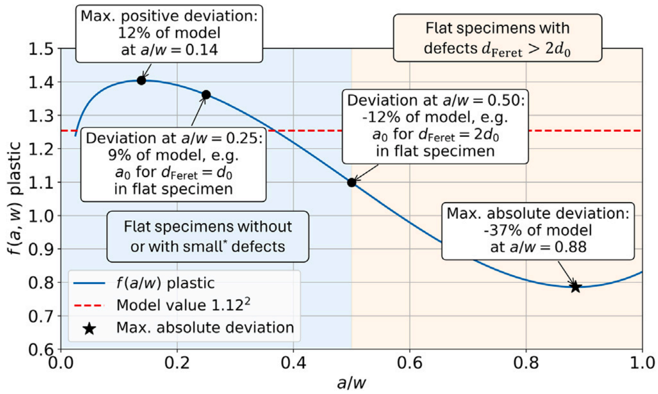

Fig. 26. Estimation of the geometry function $f(a, w)$ for the fully plastic case, compared to the geometry factor 1.12^2 used in the model. (*small compared to the dimensions of the flat specimen).

Therefore, the fatigue life for specimens containing such large defects is assessed conservatively using Z_{D}. For flat specimens, the ratio between the gauge length of the extensometer and the specimen thickness is $l_0/w = 1$. A similar approach can be used to derive a geometry function for the elastic limit based on Y_{area} and the elastic strain–energy density, where the same tendencies hold.

Notably, the scatter of N_{i} in the probabilistic model was not calibrated and the distributions of E and R_σ were derived solely from defect-free specimens. Nevertheless, the resulting fatigue life distributions also appear reasonable for specimens containing defects (see Fig. 18).

7.3. Model limits and future extensions

The range of values observed for R_σ seems to be well accounted for by Eqs. (6) - (12) however, only $R_\varepsilon = -1$ was tested. It remains to be verified whether the influence of mean stress is correctly represented in the model for other stress and strain ratios. Creep generally plays an important role in the damaging process of Ni-based superalloys at high temperatures [81,82], possibly including creep-fatigue interaction. No dominant influence is expected for $R_\varepsilon = -1$, but for positive mean stresses it is. Since time-dependent damage is currently not taken into account by the model, a model extension to significant positive mean stresses would also have to include these time-dependent effects. A reliable quantification of defect effects at 950 °C would require a more extensive experimental campaign in future work, although the results for defect-free specimens suggest that the model may also provide good predictions at this temperature.

It is expected that taking into account the scatter of further material parameters – caused by the microstructural heterogeneity and anisotropy – could improve the capabilities of the model. However, some material parameters depend on each other. For example, when including scatter of the cyclic yield stress σ_{cy} and the hardening exponent n', not all parameter combinations are physically reasonable. Some combinations would have to be excluded. Furthermore, for a given stress–strain hysteresis, different combinations of σ_{cy}, n' and E can lead to comparable descriptions of the hysteresis – especially for small loads when only little plasticity is present. This leads to difficulties in determining the probabilities of occurrence of the characteristic parameters values from experiments and, in general, to a much more complex model. Grain size and orientation were investigated in this study and are understood to be the cause of the observed scatter of the material parameters used. A direct consideration of grain parameters instead of material parameters in the model could be desirable. However, considerably more data is required for this. Such data could be obtained, for example, by means of a multitude of EBSD sections across the specimen thickness. Depending on the expected number of grains, mean and standard deviation of Young's modulus could possibly be computed using a unified scaling law following Böhlke et al. [83]. Furthermore, the model currently assumes homogeneous distributions of stress and strain, which is not the case in reality. Krause and Böhlke [84] suggested a method that yields closed-form analytical expressions to estimate stress and strain distributions in heterogeneous materials like polycrystals, that could find future application in this case as well. Another useful addition to the model could be embedding it in a more holistic probabilistic concept. This could include occurrence probabilities of certain loads, temperatures or defect sizes and could also be extended by defect detection probabilities during non-destructive testing of a part or its inspection intervals. When applying the method to a component, however, the challenge remains to translate defect indications (specific to the non-destructive testing method used) to a two-dimensional defect representation equivalent to a fracture surface image. Extracting robust 3D defect descriptors might be more difficult than measuring defect sizes on fracture surfaces. This also raises additional conceptual questions. Any 3D descriptor must be related to the loading direction (e.g., via an appropriate projection), since a given 3D measure (such as a Feret diameter) will have different implications depending on whether it is oriented parallel or perpendicular to the applied load. Moreover, in 3D it is not a priori clear where the crack will initiate on a complex defect surface, whereas in 2D the fracture surface directly reveals the critical defect cross-section at which crack initiation and growth occurred. Here, worst case estimations depending on the load direction could be a possible first step. Work by Wiedemann [85] indicates that standard quality control CT scans may fail to capture the complete extent of existing defects. In such cases, clustering multiple adjacent defects detected in terms of defect size may be necessary for accurate life assessment.

8. Summary and conclusion

In this work, high-temperature LCF experiments at 850 °C and 950 °C were performed on both defect-free specimens and specimens containing casting defects extracted from turbine blades cast from MAR-M247. A multi-step CT and μCT extraction strategy was developed and applied to position casting defects in LCF-specimens. Additionally, specimens with artificial defects were manufactured and tested. Defects were parameterized using metrics of size (d_{Feret}, $\sqrt{\text{area}}$), shape (aspect ratio, solidity, circularity), and orientation (Feret angle), assessed from fracture surfaces by SEM and image analysis. Defect size was dominant in reducing fatigue life, while shape and orientation parameters did not significantly impact fatigue life. Microstructural heterogeneity was examined by EBSD, revealing significant variations in grain size and orientation depending on the specimen extraction position in the blade. To incorporate the influence of microstructural heterogeneity on fatigue crack initiation, a physics-based deterministic model was suggested, modeling short crack growth based on the cyclic crack tip opening displacement $\Delta CTOD$. The model includes a defect size dependent El Haddad-type threshold term. Experimentally determined specimen-specific values for Young's modulus E and stress ratio R_σ were used to incorporate the effects of strongly varying anisotropic material behavior. The model is validated against experimental data, across different defect types, specimen geometries, and load regimes. Based on this, a probabilistic framework is suggested that includes lifetime scatter due to microstructural uncertainties using a Monte Carlo simulation based on experimentally obtained distributions for E and R_σ. This enables the quantification of fatigue life distributions under realistic operating temperatures and loads while also accounting for the effects of casting defects. The proposed methodology directly addresses demands arising from a more flexible gas turbine use in decarbonized energy scenarios and can support risk-based maintenance and safe, optimized gas turbine operations.

CRediT authorship contribution statement

Jan Radners: Writing – review & editing, Writing – original draft, Visualization, Validation, Software, Project administration, Methodology, Investigation, Formal analysis, Data curation, Conceptualization. **Christoph Schweizer:** Writing – review & editing, Validation, Supervision, Software, Project administration, Methodology, Funding acquisition, Formal analysis, Conceptualization. **Stefan Eckmann:** Investigation, Data curation. **Britta Bilger:** Investigation, Data curation. **Michael Schlesinger:** Writing – review & editing, Validation, Investigation, Formal analysis, Conceptualization. **Christian Amann:** Writing – review & editing, Validation, Supervision, Resources, Funding acquisition, Conceptualization. **Peter Gumbsch:** Writing – review & editing, Supervision, Resources. **Kai Kadau:** Writing – review & editing, Validation, Supervision, Resources, Funding acquisition, Conceptualization.

Declaration of competing interest

The authors declare the following financial interests/personal relationships which may be considered as potential competing interests: All authors report that financial support was provided by Siemens Energy Global GmbH & Co KG. Christian Amann reports a relationship with Siemens Energy Global GmbH & Co. KG that includes: employment. Kai Kadau reports a relationship with Siemens Energy Inc. that includes: employment. The remaining authors declare that they have no known competing financial interests or personal relationships that could have appeared to influence the work reported in this paper.

Acknowledgments

The authors would like to express their warmest thanks to Valerie Friedmann, Sabine Oeser and Karin Hintz for their support and for conducting the SEM and EBSD measurements. The authors' deep gratitude extends to Kerstin Steinle and Niklas Flamm for carrying out the difficult, non-standard specimen extraction. This work has been supported by the German Federal Ministry for Economic Affairs and Climate Action through the grant number 03EE5013H. Siemens Energy Global GmbH & Co. KG contributed financial support as an industry partner within the framework of this grant.

Federal Ministry
for Economic Affairs
and Energy

Data availability

The datasets generated and analyzed during the current study are not publicly available due to commercial confidentiality agreements with Siemens Energy Global GmbH & Co. KG. Loads are normalized by the reference strain ε_0, and all length-related quantities are normalized by the characteristic length d_0. Interested parties may direct data access requests to Siemens Energy Global GmbH & Co. KG. for consideration.

References

[1] O. Edenhofer, R. Pichs-Madruga, Y. Sokona, K. Seyboth, S. Kadner, T. Zwickel, P. Eickemeier, G. Hansen, S. Schlömer, C. von Stechow, P. Matschoss, Renewable Energy Sources and Climate Change Mitigation, Cambridge University Press, 2011, http://dx.doi.org/10.1017/CBO9781139151153.

[2] H. Breuer, in: Siemens Energy (Ed.), Ramping Up in Record Time When Sun and Wind Take a Break., 2023, URL https://www.siemens-energy.com/global/en/home/stories/ramping-up-when-the-sun-takes-a-break.html.

[3] P. Chiesa, G. Lozza, L. Mazzocchi, Using hydrogen as gas turbine fuel, J. Eng. Gas Turbines Power 127 (1) (2005) 73–80, http://dx.doi.org/10.1115/1.1787513.

[4] Press release, in: Siemens Energy, ENGIE, and Centrax (Ed.), HYFLEXPOWER consortium successfully operates a gas turbine with 100 percent renewable hydrogen, a world first., 2023-10-13, URL https://www.siemens-energy.com/global/en/home/press-releases/hyflexpower-consortium-successfully-operates-a-gas-turbine-with-.html.

[5] S.B. Narasimhachary, K. Smith, S.R. Shinde, C. Amann, K. Kadau, S. Iyer, Life assessment of large gas turbine blades, in: Proceedings of ASME Turbo Expo 2019, Volume 7A: Structures and Dynamics, American Society of Mechanical Engineers, 2019, http://dx.doi.org/10.1115/GT2019-91630.

[6] B. Ruttert, C. Meid, L. Mujica Roncery, I. Lopez-Galilea, M. Bartsch, W. Theisen, Effect of porosity and eutectics on the high-temperature low-cycle fatigue performance of a nickel-base single-crystal superalloy, Scr. Mater. 155 (2018) 139–143, http://dx.doi.org/10.1016/j.scriptamat.2018.06.036.

[7] K.D. Rekedal, Investigation of the High-Cycle Fatigue Life of Selective Laser Melted and Hot Isostatically Pressed Ti-6Al-4V, Air University, 2015.

[8] H. Masuo, Y. Tanaka, S. Morokoshi, H. Yagura, T. Uchida, Y. Yamamoto, Y. Murakami, Influence of defects, surface roughness and HIP on the fatigue strength of Ti-6Al-4V manufactured by additive manufacturing, Int. J. Fatigue 117 (2018) 163–179, http://dx.doi.org/10.1016/j.ijfatigue.2018.07.020.

[9] A. Fatemi, R. Molaei, J. Simsiriwong, N. Sanaei, J. Pegues, B. Torries, N. Phan, N. Shamsaei, Fatigue behaviour of additive manufactured materials: An overview of some recent experimental studies on Ti-6Al-4V considering various processing and loading direction effects, Fatigue Fract. Eng. Mater. & Struct. 42 (5) (2019) 991–1009, http://dx.doi.org/10.1111/ffe.13000.

[10] M. Šmíd, V. Horník, L. Kunz, K. Hrbáček, P. Hutař, High cycle fatigue data transferability of MAR-M247 superalloy from separately cast specimens to real gas turbine blade, Metals 10 (11) (2020) 1460, http://dx.doi.org/10.3390/met10111460.

[11] J. Radners, C. Schweizer, S. Eckmann, M. Al-Ameri, C. Amann, P. Gumbsch, K. Kadau, Influence of casting defects on the low cycle fatigue performance of MAR-M247 – a path towards a probabilistic model, in: Proceedings of ASME Turbo Expo 2023, Volume 11B: Structures and Dynamics, American Society of Mechanical Engineers, 2023, http://dx.doi.org/10.1115/GT2023-101940.

[12] J. Radners, C. Schweizer, M. Schlesinger, S. Eckmann, M. Al-Ameri, C. Amann, P. Gumbsch, K. Kadau, Influence of shape and size of casting defects on the LCF performance of MAR-M247 – a path towards a probabilistic model, in: Proceedings of ASME Turbo Expo 2024, Volume 10B: Structures and Dynamics, American Society of Mechanical Engineers, 2024, http://dx.doi.org/10.1115/GT2024-124232.

[13] K.N. Smith, P. Watson, T.H. Topper, Stress- strain function for the fatigue of metals, J. Mater. 5 (4) (1970) 767–778.

[14] L.F. Coffin, A study of the effects of cyclic thermal stresses on a ductile metal, J. Fluids Eng. 76 (6) (1954) 931–949, http://dx.doi.org/10.1115/1.4015020.

[15] S.S. Manson, Fatigue: A complex subject—Some simple approximations, Exp. Mech. 5 (4) (1965) 193–226, http://dx.doi.org/10.1007/BF02321056.

[16] P. Chowdhury, H. Sehitoglu, Mechanisms of fatigue crack growth – a critical digest of theoretical developments, Fatigue Fract. Eng. Mater. Struct. 39 (6) (2016) 652–674, http://dx.doi.org/10.1111/ffe.12392.

[17] J. Schijve, Four lectures on fatigue crack growth, Eng. Fract. Mech. 11 (1) (1979) 169–181, http://dx.doi.org/10.1016/0013-7944(79)90039-0.

[18] J. Polák, Cyclic deformation, crack initiation, and low-cycle fatigue, in: Comprehensive Structural Integrity, Elsevier, 2003, pp. 1–45, http://dx.doi.org/10.1016/B978-0-12-803581-8.00890-0.

[19] G. Maier, Mikrostruktur, verformung und lebensdauer der legierung alloy 617b, in: Experimente, Modelle und Bauteilvorhersagen, (407 2013) Zugl.: Karlsruhe, Inst. für Technologie, Fak. Maschinenbau, Diss., 2013.

[20] P. Neumann, New experiments concerning the slip processes at propagating fatigue cracks - 1, Acta Metall. 22 (9) (1974) 1155–1165, http://dx.doi.org/10.1016/0001-6160(74)90071-6.

[21] C. Schweizer, Physikalisch basierte Modelle für Ermüdungsrisswachstum und Anrissüberdauer unter thermischen und mechanischen Belastungen, 2013, Zugl.: Karlsruhe, Inst. für Technologie, Fak. Maschinenbau, Diss., 2013.

[22] L. Serrano, A. Scholz, F. Müller, C. Berger, C. Schweizer, M. Schlesinger, S. Eckmann, Rissverhalten unter anisothermen Beanspruchungsbedingungen – Berechnungsverfahren für Nickelbasislegierungen., 2011.

[23] W. Schmitt, R. Mohrmann, H. Riedel, A. Dietsche, A. Fischersworring-Bunk, Modelling of the fatigue life of automobile exhaust components, in: Proceedings of the Eighth International Fatigue Congress (Fatigue 2002), 2002.

[24] C.F. Shih, Relationships between the J-integral and the crack opening displacement for stationary and extending cracks, J. Mech. Phys. Solids 29 (4) (1981) 305–326, http://dx.doi.org/10.1016/0022-5096(81)90003-X.

[25] C. Schweizer, T. Seifert, H. Riedel, Simulation of fatigue crack growth under large scale yielding conditions, J. Phys.: Conf. Ser. 240 (2010) 1–4, http://dx.doi.org/10.1088/1742-6596/240/1/012043.

[26] T. Seifert, C. Schweizer, M. Schlesinger, M. Möser, M. Eibl, Thermomechanical fatigue of 1.4849 cast steel – experiments and life prediction using a fracture mechanics approach, Int. J. Mater. Res. 101 (8) (2010) 942–950, http://dx.doi.org/10.3139/146.110363.

[27] J.W. Hutchinson, Singular behaviour at the end of a tensile crack in a hardening material, J. Mech. Phys. Solids 16 (1) (1968) 13–31, http://dx.doi.org/10.1016/0022-5096(68)90014-8.
[28] J.R. Rice, A Path Independent Integral and the Approximate Analysis of Strain Concentration by Notches and Cracks, J. Appl. Mech. 35 (2) (1968) 379–386, http://dx.doi.org/10.1115/1.3601206.
[29] W. Ramberg, W.R. Osgood, Description of Stress-Strain Curves by Three Parameters, Tech. Notes No. 902- Natl. Advis. Comm. Aeronaut. (1943).
[30] V. Kumar, M.D. German, C.F. Shih, in: Electric Power Research Institute (Report) EPRI-NP-1931, Project 1237-1 (Ed.), An Engineering Approach for Elastic Plastic Fracture Analysis, 1981, http://dx.doi.org/10.2172/6068291.
[31] H. Heitmann, Betriebsfestigkeit Von Stahl: vorhersage Der Technischen Anrisslebensdauer Unter Berücksichtigung Des Verhaltens Von Mikrorissen., RWTH Aachen, 1983.
[32] W. Elber, Fatigue crack closure under cyclic tension, Eng. Fract. Mech. 2 (1) (1970) 37–45, http://dx.doi.org/10.1016/0013-7944(70)90028-7.
[33] H. Riedel, Fracture at High Temperatures, Springer Berlin Heidelberg, 1987.
[34] J.C. Newman, A crack opening stress equation for fatigue crack growth, Int. J. Fract. (24) (1984) R131–R135, http://dx.doi.org/10.1007/BF00020751.
[35] K. Kadau, M. Enright, C. Amann, Probabilistic lifing, in: N. Meyendorf, N. Ida, R. Singh, J. Vrana (Eds.), Handbook of Nondestructive Evaluation 4.0, Springer Nature Switzerland, 2025, pp. 617–654, http://dx.doi.org/10.1007/978-3-031-84477-5_11.
[36] S. Romano, S. Beretta, S. Foletti, LCF response of AlSi10Mg obtained by additive manufacturing, in: Proceedings of the Eighth International Conference on Low Cycle Fatigue (LCF8), 2017, pp. 53–58.
[37] B. Torries, R. Shrestha, A. Imandoust, N. Shamsaei, Fatigue life prediction of additively manufactured metallic materials using a fracture mechanics approach, in: Proceedings of the 29th Annual International Solid Freeform Fabrication Symposium – an Additive Manufacturing Conference, 2018, pp. 1181–1190.
[38] R. Shrestha, J. Simsiriwong, N. Shamsaei, Fatigue behavior of additive manufactured 316L stainless steel parts: Effects of layer orientation and surface roughness, Addit. Manuf. 28 (2019) 23–38, http://dx.doi.org/10.1016/j.addma.2019.04.011.
[39] S. Romano, L. Patriarca, S. Foletti, S. Beretta, LCF behaviour and a comprehensive life prediction model for AlSi10Mg obtained by SLM, Int. J. Fatigue 117 (2018) 47–62, http://dx.doi.org/10.1016/j.ijfatigue.2018.07.030.
[40] C. Fischer, C. Schweizer, Lifetime assessment of the process-dependent material properties of additive manufactured AlSi10Mg under low-cycle fatigue loading, MATEC Web Conf. 326 (2020) 1–10, http://dx.doi.org/10.1051/matecconf/202032607003.
[41] Y. Murakami, Metal fatigue, second ed., Academic Press an imprint of Elsevier, 2019.
[42] G. Liu, S. Winwood, K. Rhodes, S. Birosca, The effects of grain size, dendritic structure and crystallographic orientation on fatigue crack propagation in IN713C nickel-based superalloy, Int. J. Plast. 125 (2020) 150–168, http://dx.doi.org/10.1016/j.ijplas.2019.09.010.
[43] K. Tang, Z. Du, B. Wu, J. Hou, Fatigue behavior prediction of metal alloys based on a unified multiscale crack growth model, Eng. Fract. Mech. 235 (2020) http://dx.doi.org/10.1016/j.engfracmech.2020.107132.
[44] X. Zhu, C. Gong, Y.-F. Jia, R. Wang, C. Zhang, Y. Fu, S.-T. Tu, X.-C. Zhang, Influence of grain size on the small fatigue crack initiation and propagation behaviors of a nickel-based superalloy at 650 ° C, J. Mater. Sci. Technol. 35 (8) (2019) 1607–1617, http://dx.doi.org/10.1016/j.jmst.2019.03.023.
[45] Y. Zhang, W. Qiu, H.-J. Shi, C. Li, K. Kadau, O. Luesebrink, Effects of secondary orientations on long fatigue crack growth in a single crystal superalloy, Eng. Fract. Mech. 136 (2015) 172–184, http://dx.doi.org/10.1016/j.engfracmech.2015.01.027.
[46] Y. Zhang, H.-J. Shi, J. Gu, C. Li, K. Kadau, O. Luesebrink, Crystallographic analysis for fatigue small crack growth behaviors of a nickel-based single crystal by in situ SEM observation, Theor. Appl. Fract. Mech. 69 (2014) 80–89, http://dx.doi.org/10.1016/j.tafmec.2013.11.002.
[47] P. Li, B. Zhou, Y. Zhou, Z. Zhang, Effect of orientation on low-cycle fatigue behaviour of single crystal superalloys at 900 ° c, Mater. Sci. Technol. 35 (7) (2019) 767–774, http://dx.doi.org/10.1080/02670836.2019.1590503.
[48] Z. Xu, G. Li, Y. Zhou, C. Guo, Y. Huang, X. Hu, X. Li, Q. Zhu, Tension-compression asymmetry of nickel-based superalloys: A focused review, J. Alloys Compd. 945 (2023) 1–16, http://dx.doi.org/10.1016/j.jallcom.2023.169313.
[49] S.X. Li, D.J. Smith, Temperature and orientation dependence of elastic and yield properties of single crystal Nickel-base superalloy, Mater. Sci. Technol. 11 (12) (1995) 1253–1260, http://dx.doi.org/10.1179/mst.1995.11.12.1253.
[50] B. Engel, S. Ohneseit, L. Mäde, T. Beck, Influence of grain orientation distribution on the high temperature fatigue behaviour of notched specimen made of polycrystalline Nickel-base superalloy, Metals 11 (5) (2021) 731, http://dx.doi.org/10.3390/met11050731.
[51] B. Engel, T. Beck, N. Moch, H. Gottschalk, S. Schmitz, Effect of local anisotropy on fatigue crack initiation in a coarse grained nickel-base superalloy, MATEC Web Conf. 165 (2018) 1–8, http://dx.doi.org/10.1051/matecconf/201816504004.
[52] B. Engel, M. Huth, C. Hyde, Numerical investigation into the influence of grain orientation distribution on the local and global elastic-plastic behaviour of polycrystalline Nickel-based superalloy INC-738 LC, Crystals 12 (1) (2022) 100, http://dx.doi.org/10.3390/cryst12010100.
[53] R. Acharya, A.N. Caputo, R.W. Neu, Machine learning model for predicting the influence of crystallographic orientation on thermomechanical fatigue of Ni-base superalloys, Int. J. Fatigue 194 (2025) 1–17, http://dx.doi.org/10.1016/j.ijfatigue.2025.108832.
[54] B. Engel, L. Mäde, P. Lion, N. Moch, H. Gottschalk, T. Beck, Probabilistic modeling of slip system-based shear stresses and fatigue behavior of coarse-grained Ni-base superalloy considering local grain anisotropy and grain orientation, Metals 9 (8) (2019) 813, http://dx.doi.org/10.3390/met9080813, URL https://www.mdpi.com/2075-4701/9/8/813.
[55] Y.-T. Wu, M. Enright, H. Millwater, G. Chell, C. Kuhlman, G. Leverant, Probabilistic methods for design assessment of reliability with inspection (DARWIN), in: 41st Structures, Structural Dynamics, and Materials Conference and Exhibit, American Institute of Aeronautics and Astronautics, 2000, http://dx.doi.org/10.2514/6.2000-1510.
[56] K. Kadau, P.W. Gravett, C. Amann, Probabilistic fracture mechanics for heavy-duty gas turbine rotor forgings, J. Eng. Gas Turbines Power 140 (6) (2018) http://dx.doi.org/10.1115/1.4038524.
[57] A. de Bussac, J.C. Lautridou, A probabilistic model for prediction of LCF surface crack initiation in PM alloys, Fatigue Fract. Eng. Mater. & Struct. 16 (8) (1993) 861–874, http://dx.doi.org/10.1111/j.1460-2695.1993.tb00125.x.
[58] M.E. Melis, E.V. Zaretsky, R. August, Probabilistic Analysis of Aircraft Gas Turbine Disk Life and Reliability, National Aeronautics and Space Administration, Glenn Research Center, 1999.
[59] P. Engels, C. Amann, S. Schmitz, K. Kadau, Probabilistic fracture mechanics for mature service frame rotors, J. Eng. Gas Turbines Power 143 (7) (2021) http://dx.doi.org/10.1115/1.4049893.
[60] C. Amann, Probabilistic Fracture Mechanics of Forged Rotor Disks, (Ph.D. thesis), Karlsruher Institut für Technologie, 2017, URL https://publikationen.bibliothek.kit.edu/1000071647/4319247.
[61] P. Paris, F. Erdogan, A critical analysis of crack propagation laws, J. Basic Eng. 85 (4) (1963) 528–533, http://dx.doi.org/10.1115/1.3656900.
[62] M. Harder, P. Lion, L. Mäde, T. Beck, H. Gottschalk, Probabilistic modeling of LCF failure times using a epidemiological crack percolation model, in: 8th European Congress on Computational Methods in Applied Sciences and Engineering, CIMNE, 2022, http://dx.doi.org/10.23967/eccomas.2022.225.
[63] F. Radaelli, K. Kadau, C. Amann, P. Gumbsch, Probabilistic fracture mechanics framework including crack nucleation of rotor forging flaws, in: Proceedings of ASME Turbo Expo 2019, in: Structures and Dynamics, Vol. 7A, American Society of Mechanical Engineers, 2019, pp. 1–7, http://dx.doi.org/10.1115/GT2019-90418.
[64] F. Radaelli, C. Amann, A. Aydin, I. Varfolomeev, P. Gumbsch, K. Kadau, A probabilistic model for forging flaw crack nucleation processes, J. Eng. Gas Turbines Power 143 (10) (2021) 1–8, http://dx.doi.org/10.1115/1.4051426.
[65] F. Radaelli, C. Amann, A. Aydin, I. Varfolomeev, P. Gumbsch, K. Kadau, A probabilistic model for forging flaw crack nucleation processes for heavy duty gas turbine rotor operations, J. Eng. Gas Turbines Power 144 (12) (2022) 1–11, http://dx.doi.org/10.1115/1.4056044.
[66] Y. Yang, C. Amann, I. Varfolomeev, P. Gumbsch, K. Kadau, Probabilistic gas turbine rotor disk forging flaw crack nucleation model based on experimental data and plasticity-corrected stress intensity factor, in: Proceedings of ASME Turbo Expo 2025, Volume 8: Structures and Dynamics, American Society of Mechanical Engineers, 2025, pp. 1–8, http://dx.doi.org/10.1115/GT2025-151763.
[67] L. Mäde, S. Schmitz, H. Gottschalk, T. Beck, Combined notch and size effect modeling in a local probabilistic approach for LCF, Comput. Mater. Sci. 142 (2018) 377–388, http://dx.doi.org/10.1016/j.commatsci.2017.10.022.
[68] International Organization for Standardization (ISO), ISO 12106: Metallic materials – Fatigue testing – Axial-strain-controlled method, 2017.
[69] German Institute for Standardization (DIN), DIN EN ISO 7500-1: Metallic materials – Calibration and verification of static uniaxial testing machines – Part 1: Tension/compression testing machines – Calibration and verification of the force-measuring system, 2018.
[70] German Institute for Standardization (DIN), DIN EN ISO 9513: Metallic materials – Calibration of extensometer systems used in uniaxial testing, 2013.
[71] C. Spearman, The proof and measurement of association between two things, Int. J. Epidemiol. 39 (5) (2010) 1137–1150, http://dx.doi.org/10.1093/ije/dyq191, arXiv:21051364.
[72] M.H. El Haddad, K.N. Smith, T.H. Topper, Fatigue crack propagation of short cracks, J. Eng. Mater. Technol. 101 (1) (1979) 42–46, http://dx.doi.org/10.1115/1.3443647.
[73] S. Schackert, A. Bosch, M. Metzger, C. Schweizer, M. Vormwald, Erweiterte Schädigungskonzepte Für Thermomechanische Beanspruchung Unter Variablen Amplituden Und Plastischer Deformation, Fraunhofer IWM, TU Darmstadt, 2018, Abschlussbericht des Vorhabens Nr. 18842 N der Forschungsvereinigung Schweißen und verwandte Verfahren e. V. des DVS.
[74] A.H.-S. Ang, W.H. Tang, Probability Concepts in Engineering Planning and Design, Wiley, 1975.

[75] A. Birolini, Reliability Engineering, Springer Berlin Heidelberg, 2010, http://dx.doi.org/10.1007/978-3-642-14952-8.
[76] R. Nuzzo, Scientific method: statistical errors, Nature 506 (7487) (2014) 150–152, http://dx.doi.org/10.1038/506150a.
[77] R.L. Wasserstein, N.A. Lazar, The ASA statement on p -values: Context, process, and purpose, Amer. Statist. 70 (2) (2016) 129–133, http://dx.doi.org/10.1080/00031305.2016.1154108.
[78] I. Varfolomeev, S. Moroz, D. Siegele, K. Kadau, C. Amann, Study on fatigue crack initiation and propagation from forging defects, Procedia Struct. Integr. 7 (2017) 359–367, http://dx.doi.org/10.1016/j.prostr.2017.11.100.
[79] M.Y. He, J.W. Hutchinson, The penny-shaped crack and the plane strain crack in an infinite body of power-law material, J. Appl. Mech. 48 (4) (1981) 830–840, http://dx.doi.org/10.1115/1.3157742.
[80] J.R. Rice, P.C. Paris, J.G. Merkle, Some further results of J-integral analysis and estimates, in: J.G. Kaufman, J.L. Swedlow, H.T. Corten, J.E. Srawley, R.H. Heyer, E.T. Wessel, G.R. Irwin (Eds.), Progress in Flaw Growth and Fracture Toughness Testing, ASTM International, 100 Barr Harbor Drive, PO Box C700, West Conshohocken, PA 19428-2959, 1973, pp. 231–245, http://dx.doi.org/10.1520/STP49643S.
[81] J. Granacher, T. Preußler, Kriechgleichungen I - Numerische beschreibung des kriechverhaltens hochwarmfester legierungen, 1990, Abschlussbericht zum AiF-Forschungsvorhaben Nr. 6621, Institut für Werkstoffkunde Darmstadt.
[82] J. Granacher, A. Pfenning, Kriechgleichungen II - rechnergestützte beschreibung des kriechverhaltens ausgewählter hochwarmfester legierungen, 1993, Abschlussbericht zum Forschungsvorhaben Nr. 432, Institut für Werkstoffkunde Darmstadt.
[83] T. Böhlke, K. Jöchen, O. Kraft, D. Löhe, V. Schulze, Elastic properties of polycrystalline microcomponents, Mech. Mater. 42 (1) (2010) 11–23, http://dx.doi.org/10.1016/j.mechmat.2009.08.007.
[84] M. Krause, T. Böhlke, Maximum-entropy based estimates of stress and strain in thermoelastic random heterogeneous materials, J. Elasticity 141 (2) (2020) 321–348, http://dx.doi.org/10.1007/s10659-020-09786-5.
[85] T. Wiedemann, Digital Extraction and Comparative Analysis of Real Defects of Large Industrial Gas Turbine Blades using Various CT Technologies, Master Thesis, Berlin University of Applied Sciences and Technology, 2025.